Invited Article: An improved double-toroidal spectrometer for gas phase $(e,2e)$ studies

J. Lower, R. Panajotović, S. Bellm, and E. Weigold
Atomic and Molecular Physics Laboratories, RSPhysSE, Australian National University, Canberra, Australian Capital Territory 0200 Australia

(Received 5 December 2005; accepted 9 August 2007; published online 27 November 2007)

A new spectrometer is described for measuring the momentum distributions of scattered electrons arising from electron-atom and electron-molecule ionization experiments. It incorporates and builds on elements from a number of previous designs, namely, a source of polarized electrons and two high-efficiency electrostatic electron energy analyzers. The analyzers each comprise a seven-element retarding-electrostatic lens system, four toroidal-sector electrodes, and a fast position-and-time-sensitive two-dimensional delay-line detector. Results are presented for the electron-impact-induced ionization of helium and the elastic scattering of electrons from argon and helium which demonstrate that high levels of momentum resolution and data-collection efficiency are achieved. Problematic aspects regarding variations in collection efficiency over the accepted momentum phase space are addressed and a methodology for their correction presented. Principles behind the present design and previous designs for electrostatic analyzers based around electrodes of toroidal-sector geometry are discussed and a framework is provided for optimizing future devices. © *2007 American Institute of Physics.* [DOI: 10.1063/1.2813014]

I. INTRODUCTION

A detailed understanding of electron-impact-induced ionization is essential to our understanding of a broad range of physical processes. These include the behavior of plasmas, the physics and chemistry of the upper atmosphere, and the operation of gas lasers. The simplest example of this process is provided by the single ionization of an isolated atomic species. This process can be investigated experimentally by colliding electrons of well-defined momenta with isolated target atoms and measuring the momentum distributions of the reaction products. The reaction can be represented symbolically by the following equation:

$$e_p(\mathbf{q}_p) + X \rightarrow X^+(\mathbf{q}_{\mathrm{rec}}) + e_1(\mathbf{q}_1) + e_2(\mathbf{q}_2). \quad (1)$$

Here e_p represents the projectile electron of momentum $\mathbf{q}_p$, X^+ the residual ion resulting from the ionization of the target atom X and recoiling with momentum $\mathbf{q}_{\mathrm{rec}}$, and e_1 and e_2 the two free electrons resulting from the collision process of respective momenta $\mathbf{q}_1$ and $\mathbf{q}_2$. To obtain the most detailed information on this reaction, kinematically complete experiments must be performed in which the momenta of at least two of the three charged particles in the final state (comprising an ion and two electrons) are determined in a coincidence experiment.[1,2] The momentum of the third particle then follows from the law of momentum conservation. For the present spectrometer design, it is the momenta of the two final-state electrons which are determined in a so-called $(e,2e)$ experiment. Electron pairs derived from individual single-ionization events are identified by the time-correlated arrival of electrons at separate detectors.

In this article we describe the design and operation of our new high-efficiency spectrometer to study electron-impact-induced single-ionization processes. We first provide a historical account of developments and explain the theoretical considerations for designing optimized electrostatic electron momentum analyzers based around electrodes of toroidal-sector geometry. We then describe in detail the present $(e,2e)$ spectrometer utilizing analyzers of toroidal-sector geometry and explain the choice of design-parameter values. Finally, we present relative-cross-section data for elastic scattering and $(e,2e)$ ionization processes. These results demonstrate that while high levels of instrumental performance have been achieved, correcting for collection-efficiency variations in the measured angular distributions can be problematic.

In recent years there has been an escalation in the development of analyzers based around electrodes of toroidal geometry. Unfortunately, information concerning the subtleties of their design is scattered through the literature. By describing how we arrived at the present design, combining and building on the strengths of previous devices, we aim to provide a design framework for the optimization of future analyzer systems based around electrodes of toroidal-sector geometry.

II. BACKGROUND

From the pioneering days of electron spectroscopy to the present, electric fields have been employed to momentum analyze electrons. Analyzers employing an electric field as the momentum-dispersing medium rely on the fact that the degree of deflection experienced by electrons in traversing an electric field is dependent on their momentum. We note at the outset that the terms *electron momentum analyzer* and *electron energy analyzer* are often used interchangeably in literature. For all the analyzer configurations discussed in this ar-

ticle, not only are the energies of transmitted electrons uniquely determined, but also their direction of motion. Therefore, the more general term of electron momentum analyzer has been adopted throughout. Traditionally, $(e,2e)$ coincidence spectrometers comprise a pair of such electron analyzers, one for each of the two detected final-state electrons resulting from a single-ionization event. Each analyzer selects a portion of the electron flux leaving a localized interaction region, defined by the overlap of a gaseous target beam with an electron beam of well-defined energy. Electrostatic fields confined within each analyzer disperse electrons according to their momenta and focus them onto an electron detector. $(e,2e)$ electron pairs, corresponding to two electrons derived from a common electron-impact-induced ionization event, are identified by the correlated arrival times of two electrons at separate detectors. Contributions from events corresponding to the random arrival of two electrons from different collision events, but nevertheless falling within the instrumental timing resolution, are subtracted using standard statistical techniques.[3]

Traditionally, $(e,2e)$ experiments have been characterized by very low count rates due to the difficulty of designing analyzers achieving high momentum resolution while simultaneously collecting signal over a large volume of momentum phase space. For two analyzers of respective individual collection efficiencies ε_1 and ε_2, the total $(e,2e)$ collection efficiency is proportional to the product $\varepsilon_1\varepsilon_2$. Thus, any improvement in analyzer technology can dramatically improve the sensitivity of an $(e,2e)$ spectrometer comprising two analyzers.

In first generation $(e,2e)$ spectrometers,[4,5] two separate analyzers collect electrons over a small range of emission angles and energies, with all detected $(e,2e)$ events ascribed to a discrete momentum coordinate. In this case, spectra are accumulated by sequentially scanning both the energies and the scattering angles of emitted electrons over the momentum range of interest. Second generation spectrometers are more efficient, employing analyzers which simultaneously sample events over a range of energies[6,7] or angles.[8,9] More recently, third generation spectrometers have been developed whose analyzers incorporate two-dimensional position-sensitive detectors, enabling a range of emission angles and energies to be measured in parallel.[10–16] From the measured arrival positions of electrons at the detectors, their energies and emission angles are deduced.

An alternative and extremely powerful method for measuring the momentum distribution of charged fragments resulting from ionizing collisions is that of cold target recoil ion momentum spectroscopy[17] (COLTRIMS) or the reaction microscope.[2] Here, the interaction region is immersed in an electric and/or magnetic field, and the momenta of charged reaction products are deduced from their spatial- and temporal-arrival coordinates measured on position-and-time-sensitive electron and ion detectors. The temporal electron and ion arrival coordinates are measured with respect to the time at which the ionization event from which they originated occurred. This time of ionization is deduced by employing a nanosecond-resolution pulsed projectile beam, by measuring an emitted decay photon from the residual ion, or by approximating it as the time of detection for one of the reaction fragments if its velocity is very high. The great strength of COLTRIMS is that it can measure low-energy reaction products over an extremely large solid angle of emission (up to 4π steradians in some cases) and over an energy range encompassing all energy-loss processes. These are great advantages for coincidence experiments, which have traditionally been hampered by low data-collection rates. Indeed, experiments involving the coincidence detection of more than three collision fragments are presently only feasible using COLTRIMS techniques. Furthermore, the open spectrometer design used for COLTRIMS experiments enables collision geometries to be accessed which cannot be reached by conventional analyzers due to mechanical constraints.

The main drawback of COLTRIMS is reduced momentum resolution for the measurement of high velocity particles, a problem common to all time-of-flight spectrometers. In addition, inherent to the technique are significant nonuniformities in momentum resolution over the measured range of momentum phase space. While these are not serious drawbacks in many experiments, they do pose problems in others, for example, experiments where the dynamics of the collision process depends strongly on the angular-momentum state of the final ion which is determined by resolving closely spaced fine-structure levels,[18] or in measurements where resolution of sharp angular structures is crucial to probing relativistic effects, such as for the scattering of electrons from heavy targets.[19] Moreover, high values of energy resolution and uniform angular resolution are desirable characteristics for so-called electron momentum spectroscopy measurements.[20] Here, the accurate determination of bound-state electron momentum distributions relies on precise measurement of the energy and angular distributions of fast scattered electrons.

As the studies outlined above all overlap with our areas of interest, we set out to design a new-generation electrostatic spectrometer which would provide data-collection rates for single-ionization processes comparable to its time-of-flight counterparts, while maintaining the desirable characteristics of high energy and angular resolution inherent to conventional dispersive electron spectrometers. The new spectrometer consists of a narrow-energy-width polarized-electron source and two electron analyzers. Each analyzer comprises four electrodes of toroidal-sector geometry and a seven-element retarding lens system. Measurement is performed using position-and-time-sensitive delay-line detectors and a computer automated measurement and control (CAMAC)-based data-acquisition system. Each of these components is discussed in turn in the following sections.

III. TOROIDAL ANALYZERS

A. Toroidal geometry

At the heart of the new spectrometer is a pair of two toroidal-sector analyzers which momentum analyze electron pairs derived from electron-atom or electron-molecule collisions. Historically, the most commonly used momentum-dispersive analyzers have been based around electrodes of

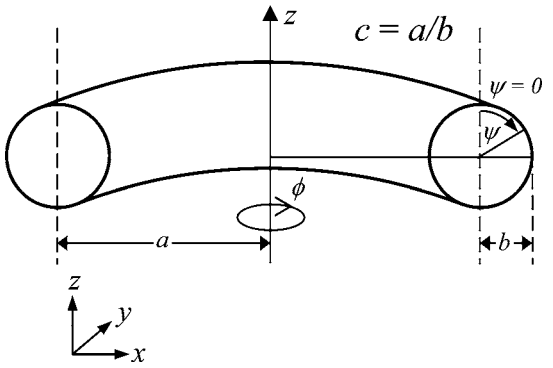

FIG. 1. The geometry of a toroidal surface is characterized by the "cylindrical radius" a and "spherical radius" b. The limiting case of the "cylindrical-to-spherical-radius ratio" $c=a/b\rightarrow 0$ corresponds to the family of spherical surfaces, while $c\rightarrow\infty$ describes cylindrical surfaces. z represents the axis of cylindrical symmetry. ϕ is the azimuthal angular displacement measured clockwise around the z axis and with respect to the positive x axis. Polar angles ψ in the radial planes are measured clockwise about the spherical-radius origin located on the positive x axis and with respect to the positive z axis.

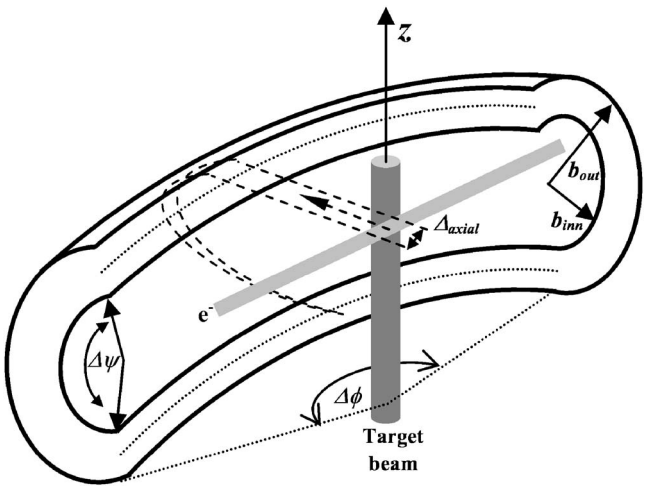

FIG. 2. A toroidal-sector analyzer comprises a pair of nested toroidal-sector electrodes spanning truncated azimuthal and polar ranges $\Delta\phi$ and $\Delta\psi$, respectively, where $0\leqslant\Delta\psi\leqslant\pi$ and $0\leqslant\Delta\phi\leqslant 2\pi$. The two electrodes are characterized by an identical cylindrical radius a, but different spherical radii b_{inn} and b_{out} (held at potentials V_{inn} and V_{out}, respectively). To first order and neglect fringing fields, electrons emanating with parallel trajectories from an extended source Δ_{axial} in the axial plane centered on the cylindrical-symmetry axis come to focus at a unique polar deflection angle $\psi_{\mathrm{axial}}(c)$ $(\equiv\Delta\psi$ in this example).

cylindrical[21,22] or spherical[23,24] geometry. Both of these geometries are, in fact, topologically related, with cylindrical and spherical surfaces representing limiting cases of the whole family of toroidal surfaces. The geometry of a toroidal surface is shown schematically in Fig. 1. It is characterized by two radii, the so-called "cylindrical radius" a and the "spherical radius" b. The shape of a particular toroidal surface is uniquely determined by the "cylindrical-to-spherical-radius ratio" c, defined by the expression $c=a/b$. The limiting case of $c\rightarrow 0$ corresponds to the family of spherical surfaces, while the limiting case $c\rightarrow\infty$ describe cylindrical surfaces.

Recently, toroidal electron analyzers of intermediate c values have become popular as they open up the possibility of parallel data collection over multiple kinematical variables. Pioneering work on the general focusing characteristics of an electrostatic field formed between electrodes of toroidal symmetry was conducted more than thirty years ago by Wollnik[25] and more recently by Toffoletto *et al.*[26] Since that time, analysis of electron-optical systems has been greatly simplified due to dramatic advances in numerical simulation techniques.

To facilitate the discussion of electrodes based on toroidal geometry and the trajectories of charged particles moving under their influence, we adopt the nomenclature of Reddish *et al.*[27] Meridian planes containing the cylindrical-symmetry axis are referred to as "radial planes," and the orthogonal planes referred to as "axial planes." Azimuthal angular displacement around the cylindrical axis is represented by the symbol ϕ, while polar angles in the radial planes are represented by the symbol ψ (see Fig. 1 and caption for detailed definitions).

B. Focusing properties of the toroidal field

"Toroidal" analyzers comprise a pair of electrodes in the shape of two toroidal-sector surfaces spanning the azimuthal range $\Delta\phi$ $(0\leqslant\Delta\phi\leqslant 360°)$ and normally the polar range $\Delta\psi$ $(0\leqslant\Delta\psi\leqslant 180°)$, as shown schematically in Fig. 2. The two electrodes are characterized by an identical cylindrical radius a, but different spherical radii b_{inn} and b_{out}. Potentials V_{inn} and V_{out} are applied, respectively, to these two electrodes with the electric field between them acting as a momentum-dispersive medium. Charged particles emerging from a localized source located on the cylindrical-symmetry axis, and at a height corresponding to the center of the interelectrode gap, are deflected and focused in the radial planes. In the limit of a point source, they experience no force components in the axial planes due to the cylindrical symmetry of the field and their azimuthal emission angles ϕ are preserved in their trajectories through the analyzer. For a small finite-dimensioned source (extent Δ_{axial} in Fig. 2), weak focusing occurs in the axial planes which strongly influences the ultimate angular resolution obtained using such an analyzer. Details concerning the focusing properties in both radial and axial planes are presented in Secs. III C and III D, respectively.

In the case of cylindrical electrodes $(c\rightarrow\infty)$, the interelectrode field varies logarithmically as a function of distance from the axis of cylindrical symmetry. For a spherical analyzer $(c\rightarrow 0)$, the field varies inversely proportional to the square of distance from the spherical-symmetry origin. In this latter case, charged particles introduced between the two electrodes travel in orbits equivalent to those describing planetary motion[28] ("Kepler orbits"). For intermediate cases $(0<c<\infty)$, the equipotentials deviate from circular symmetry in the radial planes due to curvature of the electrodes in the axial planes. In this case, the electric field is of too low symmetry for it to be determined analytically from Gauss' law and approximate analytical or numerical techniques must then be employed.[25,26] The effect is illustrated in Fig. 3 which shows equipotentials between two concentric toroidal electrodes across which a potential is applied (radial-plane

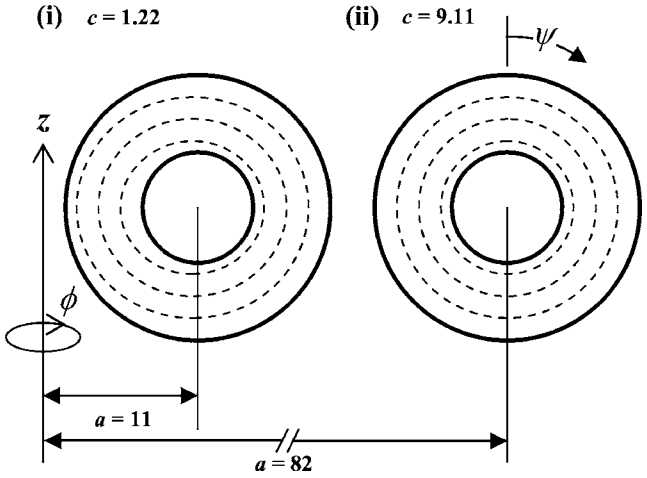

FIG. 3. A radial-plane cross section through two pairs of concentric toroidal electrodes. For each pair, the inner and outer electrodes are maintained at different potentials. The figure shows the dependence of the shape of the interelectrode equipotential surfaces on the value of the "cylindrical-to-spherical-radius ratio" c. In case (i) (small c value) significant deviations from circular symmetry are observed in the range $180° \leqslant \psi \leqslant 360°$. In case (ii) (large c value) the equipotentials are well approximated by circles.

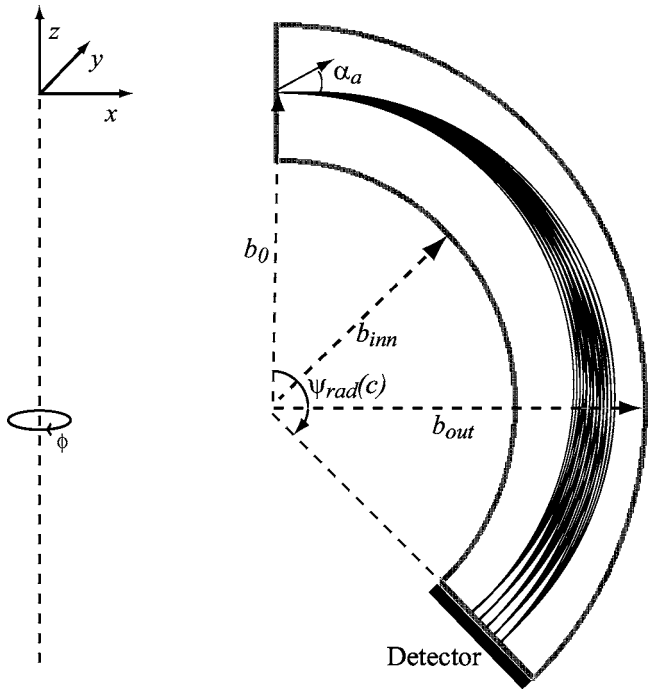

FIG. 4. Radial-plane cross section through concentric toroidal-sector electrodes showing simulated electron trajectories for the five entrance energies E_a (95, 97.5, 100, 102.5, and 105 eV) and for the entrance angles α_a of 0°, ±1°, and ±2°. The potentials V_{inn} and V_{out} applied to the inner- and outer-toroidal-sector electrodes are +52.0 and −37.1 V, respectively. Electrons of the same entrance energy, but different entrance angles, come to focus (to first order) after a deflection angle $\psi_{\text{rad}}(c)$. The effects of fringing fields have been neglected in this simulation.

cross section). In case (i), the c parameter value is close to 1.0 and significant deviations from circular symmetry are observed in the polar angular range $180° \leqslant \psi \leqslant 360°$ ($\psi=0$ taken along the positive z axis—see Fig. 1). In case (ii), $c=9.11$ and the equipotentials are well approximated by circles.

In this article, we restrict the discussion to trajectories confined to the neighborhood of a single radial plane, possessing only small out-of-radial-plane velocity components. This case pertains to the majority of recently constructed toroidal analyzers which accept electrons restricted to these so-called "polar trajectories." The possibility of exploiting the dispersive properties of the toroidal field for electrons whose main velocity components are confined to the neighborhood of a single axial plane (equatorial or radial trajectories) has been addressed previously by Wollnik[25] and will not be discussed here. As a further simplification, only the nature of trajectories originating and terminating within toroidal-sector electrodes will be considered. Expressions for electron trajectories originating and/or terminating outside the electrode boundaries can be found in Ref. 26. Furthermore, the complicating effects of fringe fields at the electrode edges, a problem common to all electrostatic analyzer designs, irrespective of whether their electrodes are based around toroidal geometry or not, will not be treated here in a quantitative fashion. However, the methods employed n the present design to minimize their influence will be discussed.

The primary aim, in any analyzer design, is to optimally exploit the focusing properties of the dispersive medium, in this case an electric field. What constitutes "optimal," however, depends upon the particular demands of a given measurement and generally involves a compromise between momentum resolution (energy and angular resolution) and the volume of momentum phase space over which measurement is performed. For the form of electrostatic field present between toroidal-sector electrodes, the nature of focusing in the radial and axial planes is distinctly different. Focusing in each is discussed separately in the next two sections.

C. Focusing in the radial planes

Figure 4 provides a schematic example of focusing in the radial planes. Here, electron trajectories, modeled by the program SIMION,[29] are shown for electrons traveling between two toroidal-sector electrodes of respective spherical radii b_{inn} and b_{out}. In this simulation, the effects of fringing fields have been neglected. Trajectories are shown for electrons originating at the mean radial position $b_0=(b_{\text{inn}}+b_{\text{out}})/2$ for five distinct analyzer entrance energies E_a (95, 97.5, 100, 102.5, and 105 eV) and for entrance angles $\alpha_a=0°, \pm1°, \pm2°$ measured with respect to the $x-z$ plane. The potentials applied to the outer (V_{out}) and inner (V_{inn}) electrodes are given in the figure caption. Trajectories corresponding to electrons of the same initial energy E_a, but different angles α_a, focus (to first order) to a common radial coordinate after a deflection angle $\psi_{\text{rad}}(c)$, whose value is determined by that of the "cylindrical-to-spherical-radius ratio" c. This property of "point-to-point" focusing enables high energy resolution and luminosity to be achieved, at the expense of averaging momentum information over a small angular range, in the present example 4°.

The deflection angle for point-to-point focusing $\psi_{\text{rad}}(c)$ increases monotonically from the limiting value of 127° for cylindrical electrodes ($c=\infty$) to 180° for spherical electrodes ($c=0$). For analyzers where trajectories originate and terminate at the edges of the toroidal-sector electrodes, $\psi_{\text{rad}}(c)$

also defines the sector angle $\Delta\psi$ of the analyzer (see Fig. 2). By approximating equipotentials in the radial plane as circular, the following expression for $\psi_{\mathrm{rad}}(c)$ can be derived:[30,31]

$$\psi_{\mathrm{rad}}(c) = \pi\sqrt{\frac{c\pi+2}{2c\pi+2}}. \tag{2}$$

For analyzers comprising two toroidal-sector electrodes, the energy resolution and the volume of momentum phase space over which measurement can be simultaneously performed is determined by the "pass energy" E_0 of the analyzer. This is defined as that particular kinetic electron energy $E_0=eV_0$ for which an electron, originating from a grounded cathode and entering the analyzer at the potential V_0 at the coordinates $(\psi=\psi_{\mathrm{init}}, r=b_0)$, will be focused to an identical radial coordinate at the analyzer exit $[\psi=\psi_{\mathrm{init}}+\psi_{\mathrm{rad}}(c), r=b_0]$. Here ψ_{init} is the polar angle which specifies the analyzer entrance plane. The value of the pass energy is determined by an appropriate choice of the potentials V_{inn} and V_{out} applied, respectively, to the inner- and outer-toroidal-sector electrodes. Assuming again circularity of the equipotential lines in the radial planes (a reasonable approximation for $0° \leqslant \psi \leqslant 180°$ and $c \geqslant 1.0$), the potentials for a given pass energy E_0 can be approximated by the expression[26]

$$V_{\mathrm{inn,out}} = V_0\left[1+\frac{2}{\pi a}(\pi a+2b_0)\left(\ln\frac{b_0(2b_{\mathrm{inn,out}}+\pi a)}{b_{\mathrm{inn,out}}(2b_0+\pi a)}\right)\right]. \tag{3}$$

The dependence of electron arrival positions at the analyzer focal surface on the magnitude of electron energy at its entrance is a monotonic nonlinear function, dependent upon the magnitudes of both the cylindrical and spherical radii and the chosen pass energy. However, for a small gap between the two electrodes comprising each toroidal-sector electrode pair, this function is well approximated by a linear relationship with a small quadratic correction. Therefore, for this electrode configuration, a planar position-sensitive electron detector positioned at the focal surface can, for a small azimuthal angular range, measure a range of electron momentum phase space with relatively uniform momentum resolution.

For a given pass energy E_0, and assuming the presence of entrance and exit slits of equal width ω through which transmitted electrons pass, the energy resolution [full width at half maximum (FWHM)] of a toroidal analyzer can be approximated by the expression[27]

$$\frac{\Delta E_{\mathrm{FWHM}}}{E_0} = \frac{\omega}{Db_0} + \kappa\alpha_{\mathrm{max}}^2. \tag{4}$$

Here, α_{max} represents the maximum value of electron entrance angle α_a (see Fig. 4). D is the dispersion given by the expression $D=(c\pi+2)/(c\pi+1)$ and $\kappa(c)$ is the aberration coefficient dependent on the "cylindrical-to-spherical-radius" parameter c. Reddish *et al.*[27] ascribe values to $\kappa(c)$ of 0.25 and 0.33 for the limiting cases of the hemispherical $(D=2)$ and the cylindrical $(D=1)$ analyzers, respectively.

For a fixed diameter of toroidal analyzer d_{tor}, where $d_{\mathrm{tor}}=a+b_0$ is the sum of its cylindrical a and mean spherical radius b_0, optimum energy resolution is achieved by maximizing the spherical radius b_0 at the expense of the mean cylindrical radius a, as it leads to increased dispersion D and decreased levels of angular aberration for focusing in the radial planes [smaller $\kappa(c)$ values]. However, the nature of focusing in the axial planes depends sensitively on the value of the c parameter and, for a given value of d_{tor}, improvements in energy resolution resulting from an increase in the value of b_0 may come at the expense of decreased angular-resolving power in the axial planes (see Secs. III D and III E).

Improvements in radial focusing can be achieved by utilizing an electrode geometry which deviates slightly from toroidal symmetry. This was demonstrated by Hellings *et al.*[32] who employed electrodes of slightly noncircular cross section in the radial planes. The exact electrode shapes were derived from solving the Laplace equation with the boundary condition that there exists, in the radial planes, an inter electrode equipotential line of circular symmetry along which the electric field is constant. Using electrode geometries derived from this procedure and which slightly deviate from toroidal symmetry, they showed that improved focusing can be achieved, not only for particles traveling in circular trajectories along a centrally located equipotential line, but also for particles of greater or smaller energy than the mean pass energy. Miron *et al.*[11] adopted this approach to develop a high-resolution electron analyzer based on two juxtaposed pairs of modified-toroidal-sector deflector plates possessing noncircular cross section. In the present design, however, our large c parameter value of 2.43 (see Sec. III E 2) meant that deviations from circular symmetry in the equipotentials were rendered small and the potential gains from adopting electrodes of noncircular cross section significantly reduced. Thus, we chose to adopt electrodes of circular cross section to simplify the manufacturing process.

D. Focusing in the axial planes

The focusing properties of the toroidal field in the axial plane are shown schematically in Fig. 2. Parallel trajectories for electrons emanating from the source of small extension Δ_{axial} in the $x-y$ plane and centered on the axis of cylindrical symmetry come to focus at a unique polar deflection angle $\psi_{\mathrm{axial}}(c)$. This property, known as "parallel-to-point" focusing,[33] is an important feature of the toroidal field which can be exploited to achieve high levels of angular (or momentum) resolution for spatially extended sources of electrons. In Fig. 2, $\psi_{\mathrm{axial}}(c)$ is shown to coincide with the chosen sector angle $\Delta\psi$ of the analyzer, although this may not necessarily be the case in any particular analyzer design. The angle $\psi_{\mathrm{axial}}(c)$ can be approximated by the expression[31]

$$\psi_{\mathrm{axial}}(c) = \pi\sqrt{\frac{c\pi+2}{8}}. \tag{5}$$

Thus, electrons emitted into the axial plane and into an arbitrary azimuthal angle ϕ' and of energy E' will, to first order, focus to a point at the polar angle $\psi=\psi_{\mathrm{axial}}(c)$, independent of their point of origin in the axial plane within the interaction region. At this polar angle, to first order, the analyzer determines azimuthal emission angles with infinitely good angular resolution, as would be the case for a point

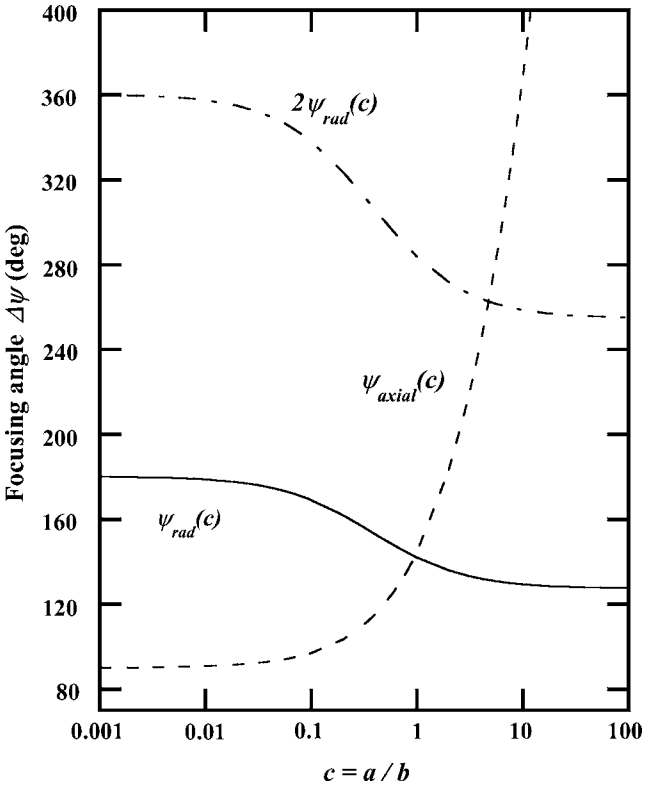

FIG. 5. Graph showing the functional dependencies of the deflection angle $\psi_{\mathrm{rad}}(c)$ for "point-to-point" focusing in the radial plane (solid line) and the deflection angle $\psi_{\mathrm{axial}}(c)$ for "parallel-to-point" focusing angle in the axial plane (dashed line) as functions of the c parameter value. Simultaneous focusing in both planes occurs at the deflection angle $\psi=142°$ for $c=0.95$. Also shown is the function $2\psi_{\mathrm{rad}}(c)$ (dash-dot curve), pertinent to the discussion of the double-toroidal analyzer, which crosses the function $\psi_{\mathrm{axial}}(c)$ at the coordinates ($\Delta\psi=262°$, $c=4.77$).

source of electrons. This property is of great significance in crossed-beam electron-atom collision experiments where the interaction region is usually of a few millimeters spatial extent in the axial plane due to the diffuse nature of effusive gaseous target beams.

Figure 5 shows the functional dependencies of both the deflection angle for "point-to-point" focusing $\psi_{\mathrm{rad}}(c)$ in the radial plane (solid line) and the deflection angle for "parallel-to-point" focusing angle $\psi_{\mathrm{axial}}(c)$ in the axial plane (dashed line) as functions of the c parameter. These two curves cross at a single unique value of $c=0.95$ corresponding to the condition and $\psi_{\mathrm{axial}}\ (c)=\psi_{\mathrm{rad}}\ (c)\sim 142°$. Thus, an analyzer constructed with this c parameter value and with a detector positioned at the polar angle of $\psi_{\mathrm{init}}+142°$ will satisfy the requirements for simultaneous focusing in both azimuthal and axial planes. This design approach has been successfully adopted by a number of groups[10,27,34] to optimize momentum resolution.

In isolation, the above considerations would uniquely recommend selection of the value $c=0.95$ for the cylindrical-to-spherical-radius ratio in any analyzer design. However, the issue is complicated by the fact that the axial angular resolution of an analyzer comprising an electrostatic lens system juxtaposed to toroidal-sector electrodes depends on the combined focusing properties of both elements. Thus, even for a selection $c=0.95$, the introduction of an electrostatic lens system between the interaction region and the toroidal-sector electrodes will modify the axial-focusing properties of the analyzer as a whole and cause a disparity between the deflection angles for "parallel-to-point" and "point-to-point" focusings. This point is discussed in more detail in Sec. III F.

Problematic to an electron analyzer employing a single pair of toroidal electrodes is that its focal surface, comprising foci at the polar angle $\psi_{\mathrm{init}}+\psi_{\mathrm{rad}}(c)$ for all transmitted electron energies and all azimuthal electron-emission angles ϕ, is a conical sector. This is problematic as modern position-sensitive charged-particle detectors are generally flat. While previous analyzers have exploited the fact that, for small range of azimuthal angles $\Delta\phi$, the conical-sector focal surface can be adequately approximated by a plane,[10,27] for larger values of $\Delta\phi$ the planar approximation is inaccurate, leading to the introduction of significant imaging aberrations. As the volume of accepted momentum phase space is proportional to $\Delta\phi$, limiting its value to reduce aberrations is not conducive to the objective of designing an efficient analyzer.

A solution to this problem, employed by a number of groups, has been to introduce optics between the exit of the toroidal electrodes and the detector and project the dispersed electron signal onto a surface located near the cylindrical-symmetry axis.[12,13,34–38] The imaging aberrations resulting from projecting particles, focusing at a conical surface, onto a planar detector are nevertheless still present. However, as the imaging aberration is now independent of the azimuthal angle ϕ, collection over an angular range $\Delta\phi$ of up to 360° can be achieved with uniform angular resolution. Nevertheless, this approach may result in nonoptimal electron detection efficiency and one possessing a ϕ dependence when microchannel-plate detectors are employed. This is because the detection efficiency for particles impinging upon microchannel-plate detectors depends strongly upon their angle of incidence, ζ, with respect to the axes of the individual microchannels which make up the microchannel plate. These axes are generally arranged with a bias angle of around 8°–15° with respect to the normal to the detector surface. For such an analyzer arrangement where electrons impact along trajectories angled away from the detector normal, ζ has a ϕ dependence [i.e., $\zeta=\zeta(\phi)$] leading to a ϕ-angle dependence in detection efficiency. While angular dependencies in collection efficiency resulting from this effect can be corrected for in software, any losses in detection efficiency will result in reduced rates of data collection. Indeed, on the basis of the work by Matsumoto *et al.*,[38] these effects may not be negligible. They reported reductions of more than 35% in detection efficiency as the angle of electron impact incident on their microchannel-plate detector varied from normal incidence over a 45° range.

In view of all of the above considerations, we adopted a different approach. We relinquished the requirement for focusing in both radial and azimuthal planes at a common deflection angle $\Delta\psi$ (so-called two-dimensional focusing) and constructed an analyzer based around four toroidal-sector electrodes. Through the choice of a large c parameter, we were able to achieve a design which (a) can be operated in

such a way to achieve an essentially planar focal surface, (b) is characterized by normal incidence of electron trajectories on to the detector surface, (c) collects simultaneously over a broad energy range, and (d), in spite of lacking two-dimensional focusing, exhibits an intrinsic insensitivity in its momentum resolution to the spatial extent of the interaction volume. The details of our approach are described in the following sections.

E. Double-toroidal analyzers

1. Background

Electron energy-analyzer designs comprising two juxtaposed pairs of toroidal electrodes have been developed by a number of groups.[11,14,32,36,39–41] The main advantage of this approach, as analyzed in the previous section, is the possibility of achieving a flat focal surface for focusing in the radial planes, rendering the analyzers compatible with planar position-sensitive electron detectors. Moreover, if microchannel-plate electron multipliers are used, the electron detection efficiency is independent of the azimuthal angle ϕ due to the normal incidence of trajectories on the microchannel-plate surface. As described previously, enhanced electron detection efficiency is generally achieved if there is approximately normal incidence of particles onto a microchannel-plate detector surface.[38]

2. Present design

The present analyzer design is shown schematically in Fig. 6. Electrons enter the analyzers in one axial plane and are focused onto a detector contained within another displaced by a distance of $3b_0$, where b_0 is the mean spherical radius. The analyzer is formed by the juxtaposition of two toroidal-sector electrode pairs, leading to a total deflection angle $\Delta\psi=\Delta\psi_1+\Delta\psi_2=270°$. Here, $\Delta\psi_1$ and $\Delta\psi_2$ are the respective polar spans of the individual toroidal-electrode pairs, with one pair spanning the range $0° \leqslant \psi \leqslant 180°$ ($\Delta\psi_1=180°$) and the other the range from $\psi=270°$ to $\psi=360°$ ($\Delta\psi_2=90°$). Respective values for the cylindrical and mean spherical radii are $a=170$ mm and $b_0=70$ mm corresponding to a c parameter value of 2.43. Values for the spherical radii b_{inn} and b_{out} are 57 and 83 mm, respectively.

Figure 6 shows simulated electron trajectories through the analyzer modeled by the program SIMION.[29] For this simulation, the respective inner- and outer-toroidal-sector electrodes for the 180° pair are held at the potentials $V_{1\text{inn}}=141.3$ V and $V_{1\text{out}}=66.6$ V and for the 90° pair at the respective potentials $V_{2\text{inn}}=282.6$ V and $V_{2\text{out}}=133.2$ V. These voltages correspond to a pass energy of 100 eV in the first toroidal-sector pair and 200 eV in the second. Unequal pass energies were selected as they were found to give better energy focusing than an equal-pass-energy combination, bringing the focal surface closer to the detector plane. Comparison of the simulation voltages with those of Eq. (3) ($V_{1\text{inn}}=141.9$ V, $V_{1\text{out}}=66.6$ V, $V_{2\text{inn}}=283.8$ V, and $V_{2\text{out}}=133.1$ V) shows agreement of better than 1%. Five different scattered electron energies (95, 97.5, 100, 102.5, and 105 eV) and a range of scattered electron emission angles α_i between ±1.4° are considered (see figure caption for details).

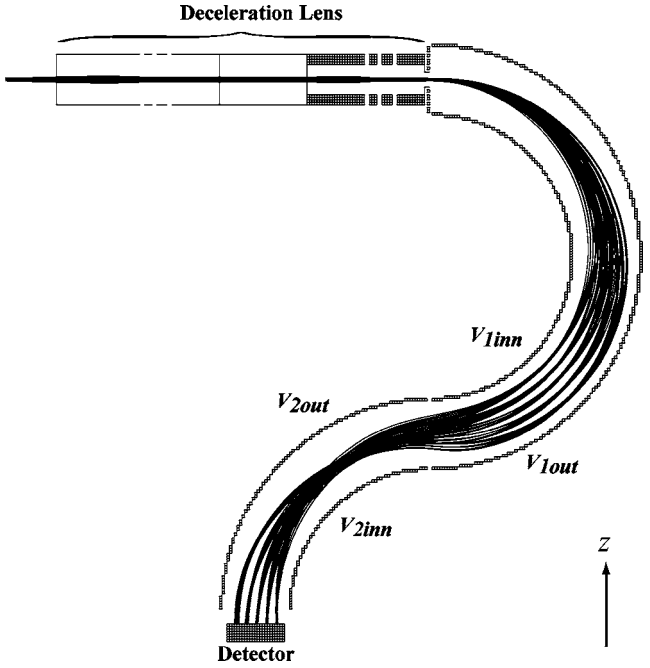

FIG. 6. Simulated electron trajectories through the present double-toroidal analyzer. Electrons emitted in the scattering plane are deflected through 270° and focused on to a position-sensitive delay-line detector from which their emission energies E, azimuthal emission angles ϕ, and arrival-time coordinates t are deduced. Trajectories corresponding to five different scattered electron energies E_i (95, 97.5, 100, 102.5, and 105 eV) and five different polar entrance angles ($\alpha_i=0°, \pm 1°, \pm 1.4°$) are shown for the pass energy $E_0=100$ eV. The inner- and outer-toroidal-sector electrodes for the 180° pair are held at the respective potentials $V_{1\text{inn}}=141.3$ V and $V_{1\text{out}}=66.6$ V and for the 90° pair at the respective potentials $V_{2\text{inn}}=282.6$ V and $V_{2\text{out}}=133.2$ V. For this simulation, the deceleration ratio $\delta_7=E_i/E_0=1.0$ was used (see text for details).

Electrons of the same energy E_i but different emission angles α_i focus twice within the radial plane, once at the polar angle $\psi_{\text{rad}}(c)=134°$ and for a second time at the deflection angle $2\psi_{\text{rad}}(c)=268°$ just before the detector. Thus, electrons leaving the "scattering plane," defined as the plane containing the momentum vectors for the incident and measured scattered electrons, are focused approximately at the detector surface.

Our present $(e,2e)$ spectrometer employs two of these analyzers. One analyzer spans the azimuthal range $\phi=285° \rightarrow 355°$ and the second the range $\phi=5° \rightarrow 135°$, where ϕ is measured with respect to the direction of the primary electron beam (directed along the positive x axis) and clockwise around the z axis (see Fig. 1). Annular electrodes, formed on printed circuit boards and held at appropriate potentials to approximate the toroidal-symmetry electric field, are used to terminate the analyzers at the azimuthal limits of $\phi=5°$, 135°, 285°, and 355° to reduce the effects of fringe fields. Approximate correction for fringe fields occurring at the lens edges is also achieved by electrodes formed on printed circuit boards, with details described in Sec. III F 3.

Due to the limited size of our microchannel-plate detectors (80 mm diameter), we can presently only measure over a 40° azimuthal band in the $5° \rightarrow 135°$ analyzer at any given time. However, the mean angular position of its detector can be adjusted from outside of the vacuum chamber to enable measurement over any arbitrary angular band between 20°

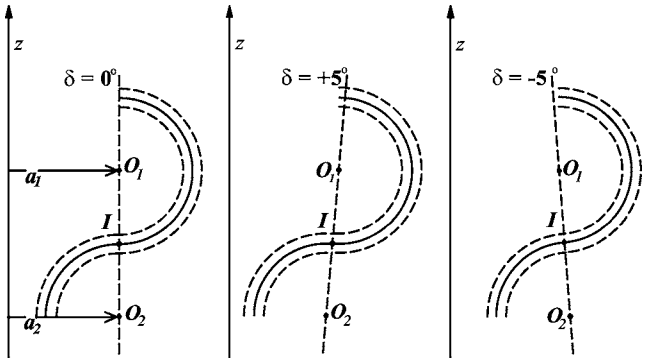

FIG. 7. Schematic representation of alternative analyzer designs for different values of the angular variable δ (see text for details). Each design comprises two toroidal-sector electrode pairs of respective cylindrical radii a_1 and a_2 and respective polar sector angles $\Delta\psi_1$ and $\Delta\psi_2$. Continuity between inner- and outer-electrode surfaces is maintained by the collinearity of the spherical radius origins (O_1 and O_2) and I, the point where the central electron path intersects the interface between the two electrode pairs. Only for $\delta=0°$ is $a_1=a_2=a$.

and 120°. The detector in the smaller toroidal analyzer is fixed in position and measures over the azimuthal range $\phi=300° \rightarrow 340°$.

For both analyzers, electrons are blocked from entering within 15° of their azimuthal angular limits. This precaution was taken as any uncorrected fringe-field components in the vicinity of the analyzer limits could adversely affect electron trajectories and lead to distortions in angular distributions. Furthermore, this step helps in suppressing off-axis contributions from electrons scattered from background gas along the length of the primary electron beam from colliding with the sides of the lens system and the analyzer (see Sec. VII).

3. Optimization of design parameters

Designing a double-toroidal analyzer which exhibits a flat (or approximately flat) focal surface for radial focusing and achieves a suitable balance between energy resolution, angular resolution, and collection efficiency is not a simple exercise. As described by Miron *et al.*,[11] the values of c, $\Delta\psi$, $\Delta\psi_1$, and $\Delta\psi_2$ must all be adjusted in a constrained manner to obtain an optimized focusing performance. This is nontrivial, as changing the value of any of these variables redefines the constraints on the possible values for the others. Assuming an identical spherical radius b_0 for both toroidal-sector electrode pairs, continuity between the inner- and outer-electrode surfaces can be ensured by enforcing collinearity of the two spherical-radii origins and the point where the central electron path intersects the interface between the two electrode pairs.[11] This is illustrated schematically in Fig. 7. Under such a constraint, and for an analyzer designed to accept electrons emitted into a common plane, if the total deflection angle $\Delta\psi=270°$ is varied by a small amount 2δ, then $\Delta\psi_1$ and $\Delta\psi_2$ must be constrained by the requirements that $\Delta\psi_1=180°+\delta$ and $\Delta\psi_2=90°+\delta$. As δ is increased from zero, the cylindrical radii a_1 and a_2 for both sectors [and their respective c and $\psi_{\mathrm{rad}}(c)$ parameters] deviate from a common value. In this case, the displacement of the four sectors from the cylindrical-symmetry (z) axis must be adjusted to maintain radial focusing at the total deflection angle $270°+2\delta$ (i.e., at the detector plane). It should be noted that both the angular and energy resolutions of the device are affected by the changes to the value of δ. In the former case, this arises primarily from changing the distance a_2 at which the image is projected from the symmetry axis. In the latter case, changes to the value of δ sensitively affect the dispersion of electron energies with position at the analyzer exit plane through modifications to electron trajectories.

The present design parameters were selected on the basis of simulation and from our understanding of the focusing properties of toroidal-symmetry electrostatic fields at the time. Solving the equation $\psi_{\mathrm{rad}}(c)=135°$ [Eq. (2), Fig. 5] for our chosen δ value of 0.0 gives the value $c=2.29$, indicating in retrospect that our chosen c value of 2.43 was not optimal but some 8% too high. Furthermore, we believe that more extensive simulations would have revealed improved focusing for a slightly nonzero value for δ. Fortunately, experiment has since confirmed that the adverse effects of the present displacement between the surface for radial focusing and the detector plane can be partially compensated for through adjustment of the input electron optics and operation of the two toroidal-sector electrode pairs at unequal pass energies.

Problematic to the double-electrode-pair configuration, relative to its single-pair counterpart, is the necessity of adopting a large c parameter value to achieve both two-dimensional focusing and a flat focal surface. This is illustrated in Fig. 5 where $2\psi_{\mathrm{rad}}(c)$ (dash-dot curve) and $\psi_{\mathrm{axial}}(c)$ (dashed curve) are plotted as a function of the c parameter. The two curves uniquely cross at the coordinates ($\Delta\psi=262°$, $c=4.77$). Thus, by choosing a value of δ around 4° and by adjusting the c parameters as described above, it should be possible to at least approximately satisfy both the conditions for two-dimensional focusing and a flat focal surface simultaneously. However, such a combination of a small spherical radius with a large cylindrical radius is not conducive to obtaining high-energy resolution for a given analyzer size d_{tor}, as discussed in Sec. III C.

4. Angular resolution considerations

In the present design, a considerably smaller c parameter value of $c=2.43$ was chosen to improve the energy resolution and to project electrons closer to the symmetry axis so a larger azimuthal angular range could be intercepted by our 80 mm detectors. Substitution of $c=2.43$ into Eq. (5) gives $\psi_{\mathrm{axial}}(c)=197°$, a full 73° short of the deflection angle required to achieve two-dimensional focusing at the analyzer exit plane. Thus, electrons of the same emission energy, emanating in parallel trajectories from an extended source in the axial plane, do not focus to a point on the detector, but rather to a line. In isolation, the length of this line would determine the azimuthal angular resolution of the analyzer. However, as mentioned in Sec. III D, the angular resolution of the analyzer depends not only on the focusing properties of thetoroidal-sector fields but also on the geometry and operating voltages applied to its input electron optics. Due to

finite extent of the interaction region in the axial plane, electrons emitted into any particular azimuthal angle ϕ enter the curved lens electrodes with a small range of tangential velocity components, leading to a displacement of the mean deflection angle $\overline{\Delta\psi}_{\text{axial}}$ for parallel-to-point focusing. For the present input optics design, our simulations have shown that, for a limited set of lens voltages, $\overline{\Delta\psi}_{\text{axial}}$ can be brought to 270°, satisfying in an average way the conditions for two-dimensional focusing. Under other conditions, however, especially with larger values of deceleration, the axial angular resolution is significantly degraded by the axial-focusing effects of the lens. A more detailed discussion of this effect will be given in Sec. III F.

In spite of the lack of two-dimensional focusing in the present design, its large value of cylindrical-to-spherical-radius ratio c greatly reduces its sensitivity to small extensions of the target Δ_{axial} in the axial plane, irrespective of the chosen lens operating potentials. This is because electrons are focused at a radial distance well removed from the axis of cylindrical symmetry z (see Ref. 42). As a result, good angular resolution in the axial plane is achieved for an extended target region under a range of operating conditions (see Sec. VII).

5. Focusing aberrations in the radial planes

Problematic to the double-toroidal configuration are focusing effects introduced by the potential reversal occurring at the interface between the two toroidal-sector electrode pairs. At this location, the electrode at potential $V_{1\text{inn}}$ juxtaposes one at potential $V_{2\text{out}}$ and the electrode at potential $V_{1\text{out}}$ juxtaposes one at potential $V_{2\text{inn}}$. Figure 8 shows an expanded view of this region, with potential contour lines corresponding to (a) equal and (b) unequal pass energies for the toroidal-sector electrode pairs 1 and 2. In both cases, severe distortions of the quasicircular field lines are evident in the neighborhood of the potential reversal. Focusing aberrations result from the fact that the potential change is stepwise *only at the electrode boundaries* and not throughout the plane separating the two toroidal-sector electrode pairs (this plane is indicated by the dashed lines in Fig. 8 and is orientated perpendicular to page). These focusing aberrations reduce the resolving power of the double-toroidal analyzer to a value less than that for a single-toroidal analyzer of comparable "cylindrical" and "spherical" radii.

Case (a) is the easiest to interpret due to its higher symmetry, with the potential distribution showing approximate inversion symmetry about the dashed line separating the two toroidal-sector pairs [exact symmetry does not occur, resulting from differences in their respective equipotential surfaces due to the different polar angular ranges spanned by the two sector pairs, namely, $0° \leqslant \psi \leqslant 180°$ for sector pair 1 and $270° \leqslant \psi \leqslant 360°$ for sector pair 2 (see Fig. 3)]. Electron trajectories passing through the center of the interelectrode gap (passing through position A on figure) suffer a loss in their radial-force component over a relatively large distance as they traverse the interface. For such trajectories, and to a very good approximation, no net gain in kinetic energy is acquired as electrons traverse the interface and continue on a quasicircular arc to the detector. In contrast, higher- and lower-energy electrons, passing respectively closer to the outer and inner electrodes of toroidal sector 1 (respectively, intersecting positions B and C on Fig. 8), are accelerated with a strong force component tangential to their trajectories in the neighborhood of the potential reversal over a relatively short distance, before the quasiradially symmetric electric field is restored on either side of the interface. Initially higher-energy electrons, passing closer to the outer electrode of the electrode pair 1, experience an energy gain as they traverse the interface and arrive at the detector at a position closer to the outer electrode of toroidal-sector electrode pair 2. For initially lower-energy electrons, passing close to the inner electrode of electrode pair 1, the reverse is true. They experience a kinetic-energy loss as they traverse the interface and arrive at the detector at a position closer to the inner electrode of toroidal-sector electrode pair 2. It is this unequal treatment of electrons as a function of their radial position at the interface which causes the trajectories to cross over at a deflection angle $\Delta\psi \sim 220°$ and results in an inverted image, at the detector, of that appearing at the first focal plane. A second consequence of this unequal treatment is the introduction of an energy-dependent modification to the electron focal lengths which degrades energy resolution. Indeed,

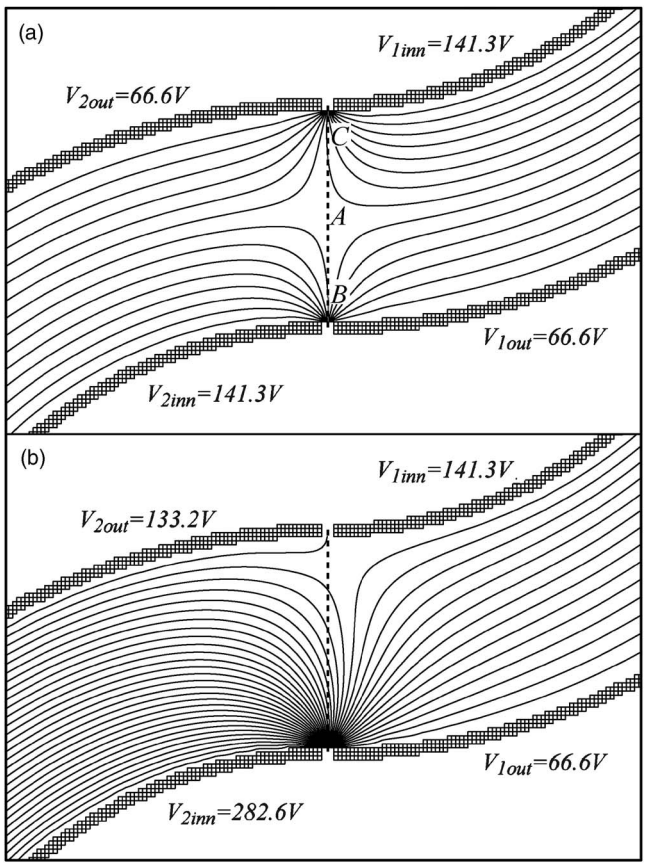

FIG. 8. Radial-plane view of the interface between the two toroidal-sector electrode pairs comprising the present double-toroidal-sector analyzer. Equipotential lines are shown for (a) the case of equal pass energies and (b) the case where the pass energy of the second toroidal-sector electrode pair is twice that of the first. For case (b), the applied potentials correspond to the simulation of Fig. 6. See text for details.

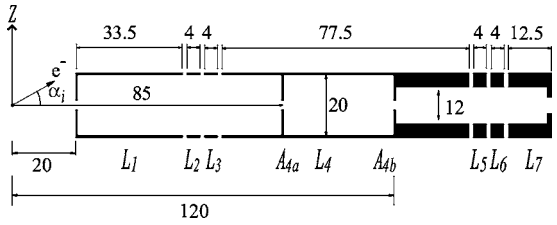

FIG. 9. The seven-element angle-resolving electrostatic lens system used to angularly select and focus electrons emitted from the interaction region at angles α_i. It consists of a grounded first lens (L_1), two defining slits A_{4a} and A_{4b}, and five focusing lenses (L_2–L_6) of independently adjustable potentials. The final lens (L_7) is fixed to a potential value determined by the analyzer pass energy E_0. Each lens comprises an identical pair of annular electrodes. Indicated dimensions are in millimeters. See text for details.

simulation predicts a reduction in resolution of around 30%–40% as a result of the presence of the second toroidal-sector pair for this case of equal pass energies.

For case (b), the pass energy for the toroidal sector electrode pair 2 is twice that of electrode pair 1, as was the case for the simulation of Fig. 6. Operating in this asymmetric mode, approximate inversion symmetry about the plane separating the two toroidal-sector pairs is no longer present. Interestingly, simulation shows that this potential configuration gives markedly superior performance than for case (a) as it has the effect of pushing the focal points for electrons of the same entrance energy closer to the detector plane than is achieved for the symmetric operation of the two toroidal-sector electrode pairs. Furthermore, acceleration of electrons at the interface between the two toroidal-sector electrode pairs also reduces divergence of trajectories through the Helmholtz-Lagrange law.[43] For case (b), simulation predicts less than a 10% reduction in energy resolution at the deflection angle of 270° compared to that at the first focal plane (deflection angle of 134°).

Finally, we note that aberrations resulting from juxtaposition of the two toroidal-sector electrode pairs decrease monotonically to zero as the relative interelectrode gap $g=(b_{\text{out}}-b_{\text{inn}})/(b_{\text{out}}+b_{\text{inn}})$ tends to zero. In spite of this fact, a large value for g, much higher than in previous designs,[11] was chosen in the present design to maximize the range of energies that could be simultaneously measured at a given pass energy. As the volume of momentum phase space accepted by the analyzer increases proportionally to $\sqrt{g}$, a compromise needs to be made between energy resolution and the volume of accepted momentum phase space in selecting an optimal value for g in any particular design scenario.

In summary, trajectories through the double-toroidal analyzer are very complicated, especially due to the effects of juxtaposing a second toroidal-sector electrode pair to the first. The authors believe that further scope exists for a deeper understanding of the focusing properties of the double-toroidal-sector analyzer and for improvements to the present analyzer design. However, this would require a much more extensive and systematic program of simulation lying beyond the scope of this work.

6. Timing resolution

In their transit through a double-toroidal analyzer, electrons focus twice in the radial planes, compared to once in analyzers based around a single-toroidal-sector electrode pair. For coincidence experiments, this doubling of electron transit length leads to a factor of 2 reduction in the instrumental timing resolution used to identify time-correlated electron pairs. Reductions in timing resolution degrade the statistical quality of acquired $(e,2e)$ data due to increased levels of measured background.[3] While the recorded electron arrival positions can be used to correct for the energy-dependent variation of flight times through the analyzer,[3,44] no correction can be made for the variations in the trajectories of electrons of the same entrance energy E_a but different entrance angles α_a, as they focus to the same location on the detector.

F. Entrance lens design

1. Background

The present design was developed using three resources. The first was the article of Kevan[7] who, for cylindrical-electrode geometry, sets out principles for designing a five-element lens system providing independent control of angular acceptance and electron deceleration in a fixed-focal-length lens. The second was our simulation using the SIMION (Ref. 29) software package, which enables the calculation and visualization of trajectories of charged particles as they traverse through an arbitrary three-dimensional electrostatic-field configuration. The third was the parameterization of lens data for cylindrical (and slit) lenses compiled by Harting and Read.[45] While the results of Kevan[7] showed that excellent performance could be obtained from a five-element variable-angle-acceptance lens system with cylinder lenses, simulation indicated that, for our annular-lens geometry, a seven-element design would provide superior operation.

2. Present design

The electrostatic lens system is shown in detail in Fig. 9. Its function is to define the analyzer's angular ($\Delta\alpha_i$) acceptance in the radial planes and to transport electrons emitted from the interaction region to the toroidal deflectors' entrance plane, in the process accelerating or decelerating them to the required pass energy E_0. It comprises a grounded first lens (L_1), five focusing lenses (L_2–L_6) of independently adjustable potentials V_2–V_6, respectively, and a terminating lens L_7 of fixed potential V_7 determined by the chosen value for E_0. Each lens comprises a pair of identically dimensioned annular electrodes concentric with the cylindrical-symmetry axis (z axis). The two electrodes in each pair are separated by 20 mm along the z axis for lenses L_1–L_3 and 12 mm for lenses L_5–L_7. For L_4, the separation changes from 20 to 12 mm separation in a stepwise manner. The mean radius of each pair increases monotonically from L_1, located adjacent to the interaction region, to L_7 which adjoins the 180° toroidal-sector pair. The gap between the individual lenses is 1.5 mm and the separation between L_7 and the 180° toroidal-sector pair is 1.5 mm.

3. Operating principles

Adapting the principles used by Kevan[7] to annular-lens geometry, our design allows adjustment to the radial-plane

angular acceptance $\Delta\alpha_i$, while maintaining a fixed object-image distance. In this case the "object" is located at the cylindrical-symmetry axis, and its angle-selected image is projected at the entrance plane of the first toroidal-sector electrode pair. These two goals are achieved by a two-stage lens system in which electrons pass through an intermediate focus within L_4.

The first lens stage comprises the four lenses L_1–L_4. Its function is to accurately define the analyzer angular acceptance $\Delta\alpha_i$ in the radial plane for electrons emerging from the interaction region (centred at $x=y=z=0$) at arbitrary angles α_i (see Fig. 9). The electrons first pass through a field-free region before entering a grounded L_1 via a 2.4 mm curved-entrance slit (center of curvature, the z axis). Angular selectivity is achieved primarily at A_{4a} (a 1.8 mm slit) located within L_4 at the so-called "Fourier transform plane" (FTP). Electrons emitted with the same polar emission angle α_i (and energy E_i, where E_i is the kinetic energy of electrons leaving a grounded interaction region), independent of their z coordinate within the interaction region, focus to a unique position $d(\alpha_i)$ measured from the x-y plane passing through the center of the lens and along the z axis at the FTP. The magnitude $|d(\alpha_i)|$ increases monotonically with increasing values of $|\alpha_i|$, with proportionality occurring for small values of $|\alpha_i|$. Positive values of α_i lead to positive values of displacement for $d(\alpha_i)$, and negative values to negative values of displacement for $d(\alpha_i)$ along the z axis. A significant design challenge was to establish a set of lens dimensions for which the FTP would be located well inside L_4 to ensure that the angle-defining slit A_{4a} would not significantly perturb the focusing fields of L_2 and L_3. This goal was achieved by employing a relatively long first lens stage.

For a given width of the angle-resolving slit A_{4a}, the magnitude of the angular acceptance can be varied by adjusting the potential of L_4 (and, hence, the kinetic energy of electrons traveling through it). This action varies the dispersion of $d(\alpha_i)$ with α_i at the FTP. When adjusting V_4, the potentials V_2 and V_3 must also be adjusted to maintain the FTP at the location of A_{4a}. Defining the intermediate deceleration ratio $\delta_4=E_i/E_4$ where $E_4=E_i+eV_4$, the greater the value of δ_4 (the more negative V_4), the smaller is the angular spread $\Delta\alpha_i$ of electrons transmitted through A_{4a}. In the absence of aberrations, these quantities are simply related through the Helmholtz-Lagrange law.[43] Also evident from Fig. 9 is a second slit A_{4b} (presently a 2 mm slit) located in L_4. Its primary function is to inhibit stray scattered electrons, which follow distinct trajectories from those undergoing a single-scattering event at the interaction volume, from entering the analyzer. However, if the dimensions of the interaction volume exceed 1 mm in the z direction, this slit also plays a role in maintaining energy resolution by reducing transmission of electron signal from the z extremities through the analyzer.

The second lens stage comprises L_4 and three additional lenses (L_5–L_7). It performs the task of focusing, in the radial plane, the angle-selected image of the interaction region at the toroidal-sector curved-entrance surface for an arbitrary analyzer pass energy E_0 (or any final deceleration ratio $\delta_7=E_i/E_0$). The potential V_7 is determined through the formula

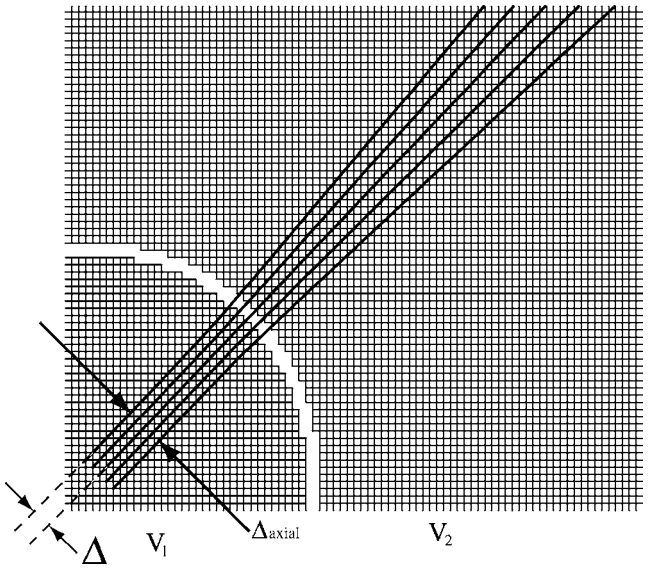

FIG. 10. Divergence of initially parallel electron trajectories as they pass between two juxtaposed pairs of annular-lens electrodes operated at different potentials (axial-plane view). The dimensions, electron energies, and potentials were chosen for illustrative purposes only. Parallel off-axial rays are deflected in the axial plane as they traverse the lens-pair interface. The degree of axial-plane deflection increases monotonically with increasing displacement Δ of the trajectory from that of an electron emanating from the axis of cylindrical symmetry into the same azimuthal scattering angle ϕ. Note that deviations shown are due to curvature of lens surfaces, not due to the apparent "discrete" nature of the simulation grid.

$V_7=(E_0-E_i)/e$. Without this second lens stage, an independent choice of both the angular resolution and the analyzer pass energy E_0 would not be possible. Having adjusted $V_2 \rightarrow V_4$ for the required angular resolution and set the appropriate value of V_7, the potentials V_5 and V_6 are then adjusted to achieve the required total object-image length of 170 mm.

To assist in correcting for fringe fields at the edges of the lenses, field-correcting plates were attached at the azimuthal angles $\phi=5°$, 135°, 285°, and 355°. Each plate comprises a matrix of square pads, with each pad connected to its neighbor by a 10 MΩ resistor. The top and bottom rows of pads at each lens edge are electrically connected to their adjacent lens plate. As a result, a field distribution at the edges of the lenses is formed which closely approximates the ideal field occurring well inside the lens boundaries.[46]

4. Axial focusing

The adoption of a large object-image distance in the first lens stage was also crucial to minimize focusing in the axial plane resulting from the axial-plane extension Δ_{axial} of the interaction region. This effect is demonstrated in Fig. 10 which shows an x-y plane projection of initially parallel electron trajectories, emanating from a source of dimension Δ_{axial}, as they pass through two juxtaposed annular-lens pairs. Lens dimensions and voltages V_1 and V_2 were chosen for illustrative purposes only. It is seen that parallel off-axial rays are deflected in the axial plane as they traverse the lens interface, with the degree of deflection increasing with increased displacement Δ from the cylindrical-symmetry axis.

While such axial-focusing effects are unavoidable, they can be reduced by minimizing the quantities $\Delta_{\text{axial}}/r_i$, where

FIG. 11. Double-toroidal-sector electron analyzer (lens system removed). For clarity, field correcting side plates which assist in correcting for fringe fields at the edges of both the lens system and toroidal-sector analyzer have also been removed. Supporting bar, is for structural stability only, and is removed when side plates are in place. See text for details.

r_i are the radial distances measured from the z axis to the interfaces between lenses L_i and L_{i+1}. In particular, minimization of this quantity is crucial in the first lens stage where r_i values ($i=1-3$) are smaller and the electron velocity components tangential to the curved lens interfaces are larger. In the present design, the relatively large adopted values of r_1 and r_2 minimize this effect. Nevertheless, at larger values of deceleration ($\delta_4 \geqslant 4$), simulations show that the above effect can degrade angular resolution beyond 4° FWHM for $\Delta_{\text{axial}} > 2$ mm.

G. Analyzer construction

The present toroidal-sector electrodes are shown in Fig. 11. The electrodes were manufactured by turning aluminum blocks to the required spherical and cylindrical radii before cutting them to their prescribed sector angles. The lens plates were turned from 310 stainless steel and cut into their respective azimuthal sectors using a wire cutter. Stainless steel screws and alumina insulators were used to secure together all components and electrically isolate them from one another.

IV. THE ANU (*e*,2*e*) SPECTROMETER

Figure 12 shows a schematic representation of the present spectrometer comprising two toroidal-sector electron analyzers and a polarized-electron beam source. The original beam-source design, significantly modified for the present application,[19] was based on that of Pierce *et al.*[47] More recent discussions on the operation and potentialities of polarized-electron beam sources are described in the literature.[48,49] For clarity, only the azimuthal capture range of the two toroidal analyzers is shown. An electron beam is

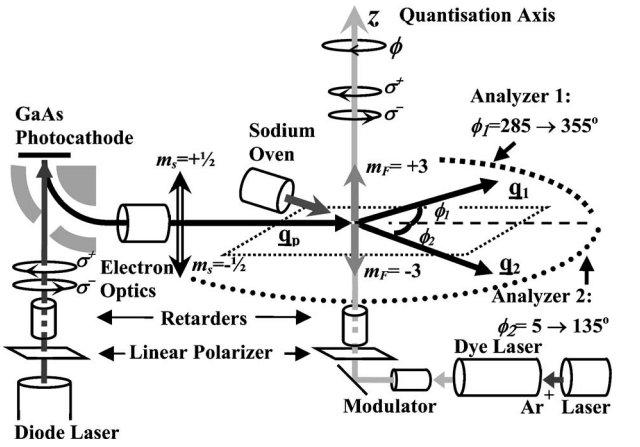

FIG. 12. Schematic representation of the polarized-electron (*e*,2*e*) spectrometer comprising polarized-electron source, two double-toroidal-sector electron analyzers, and a Mott polarimeter (not shown). See text for details.

created by the photoexcitation, and subsequent extraction, of electrons from a strained gallium arsenide crystal under illumination by circularly polarized photons. Circularly polarized radiation is produced by passing the light from a laser diode (Roithner RLT8520MG) through a linear polarizer followed by a liquid crystal retarder (Meadowlark model LVR 100). By orienting the polarization axis of the laser light at 45° to the retarder axis and setting the retardance value to either $+\lambda/4$ or $-\lambda/4$, radiation of right- or left-hand helicity is, respectively, produced. The magnitude of retardance is set by the retarder controller (Meadowlark model B1020) which itself is under computer control.

Due to the electronic structure of the GaAs photocathode, illumination by right-hand helicity radiation gives rise to electrons preferentially polarized parallel to the extraction direction, while illumination by left-hand helicity radiation produces electrons polarized preferentially in an antiparallel direction.[50] The structure of the photocathode, manufactured at the ANU,[51] is similar to that described previously[52] where values of up to 80% electron spin polarization were achieved. In the present case, however, only (50±4)% spin polarization is achieved at a laser wavelength of 850 nm. The reason for the lower than expected value of polarization is presently unclear; however, it still represents a considerable improvement over the 24% reported in our earlier measurements.[18]

After extraction, the spin-polarized photoelectrons are deflected through 90° by an electrostatic field to produce a beam of transversely polarized electrons. Transverse polarization is a necessary condition[18] to observe nonzero spin effects in the present reaction geometry in which the momentum vectors for the incident and detected scattered electrons are confined to a common plane (the so-called scattering plane). The electron beam is then accelerated to around 1 keV of energy and transported at high energy through a differential-pumping stage before entering the collision chamber in which the toroidal electron analyzers are housed. The collision chamber is evacuated by a combination of a diffusion and a turbopump of combined 1000 l/s pumping speed. Inside the collision chamber, the electron beam is then decelerated to energy E_p utilizing a five-element electrostatic

lens and focused on to a beam of target gas at ground potential. The overlap of electron and target beams defines a localized interaction volume. The required collision energy $E_p = -eV_c$ is set by adjusting the photocathode potential V_c.

Depending upon the nature of the experiment, the gaseous target beam is formed in either one of two ways. For nonmetallic species, it is produced by effusion through a 10 mm long, 0.7 mm bore molybdenum tube which terminates 1 mm below the scattering plane. In this case, the target-beam axis is collinear with the axis of cylindrical symmetry (z axis). For metallic target species, a recirculating metal-vapor oven is employed.[53] In this case, atoms effuse through a 1 mm diameter circular aperture, with the atomic beam constrained to the x-y scattering plane and directed towards the z axis. For those experiments in which laser-pumped excited and/or oriented atomic target states are of interest, a second laser system is employed comprising a Coherent CR-699-21 ring dye laser pumped by a Coherent Innova 300 argon ion laser. The spin polarization of the target ensemble and its angular-momentum orientation[54] (each either into, or out of the scattering plane) are controlled by the reversing the helicity of dye laser light through the actions of a linear polarizer and $\frac{1}{4}$-wave retarder introduced between the dye laser and the interaction region.[53]

Electrons scattered within the x-y plane are momentum analyzed in one of the two double-toroidal-sector electrostatic energy analyzers, one located on each side of the primary electron beam. Measurements are restricted to $(e,2e)$ events falling within the angular and energy acceptance ranges of the two toroidal analyzers, namely, $285° \leqslant \phi_1 \leqslant 355°$, $5° \leqslant \phi_2 \leqslant 135°$, $\Delta E_1 = E_1 \pm 0.1E_0$, and $\Delta E_2 = E_2 \pm 0.1E_0$. With the presently employed detection electronics (single-hit time-to-digital converters), only those ionization events are measured for which members of each $(e,2e)$ electron pair are detected in separate analyzers.

V. ELECTRON DETECTORS AND PROCESSING ELECTRONICS

A schematic representation of the detectors and their associated signal-processing electronics is shown in Fig. 13. Electrons transmitted through the toroidal analyzers are focused onto the electron detectors. The detectors each comprise two chevron-mounted microchannel-plate electron multipliers[55] (MCPs), followed by a two-dimensional crossed-delay-line detector[17] from which electron arrival positions (x,y) are derived. An electron impinging on the first microchannel plate in each pair induces an electron cascade which results in a cloud of around 10^6 electrons emerging from the back surface of the second plate within a fraction of a nanosecond. This cloud is then collected on the positively biased crossed-delay-line detector from which its average arrival coordinate $(x,y)_{av}$ is deduced. The value $(x,y)_{av}$ is then used to accurately approximate the (x,y) arrival position of the electron which instigated the cascade.

The delay-line detectors consist of two orthogonally orientated, helically wound wire pairs. One pair is used to determine the x coordinate, and the other the y coordinate of the arriving electron clouds. In each pair, one wire is positively biased with respect to the other and efficiently collects the cloud electrons. The x (or y) arrival coordinate of each electron cloud can then be determined from the relative arrival times of the resulting charge pulses traveling towards the two ends of this wire. The second wire in each pair, being less positively biased, picks up only electrical noise. Signals measured from its two ends are used for noise suppression. Pulses from the two delay-line collection wires, along with noise collected on their respective reference wires, are measured in four differential-amplifier/constant-fraction discriminator units (RoentDek model DLATR6). These units amplify the signals and produce fast output pulses, time correlated to true cascade-related input pulses.

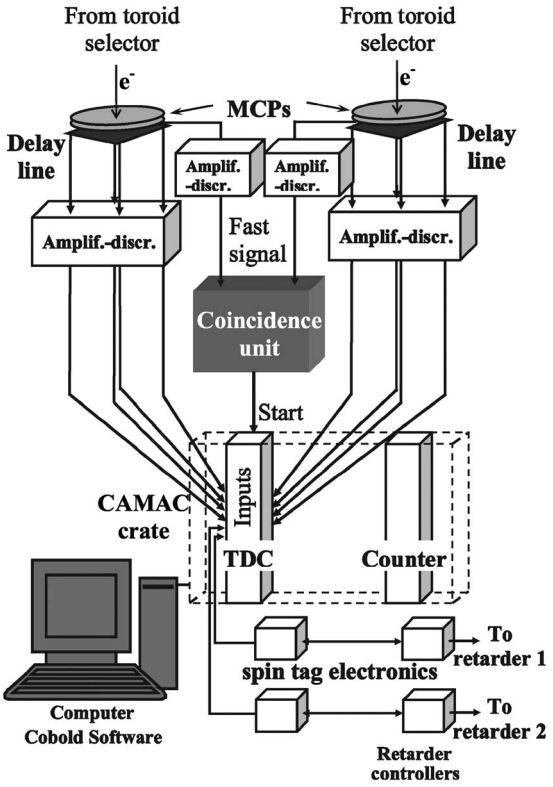

FIG. 13. Schematic representation of the electron detection and instrumental control electronics. It comprises microchannel-plate electron multipliers (MCP), two delay-line position-and-time-sensitive detectors, amplifiers, and discriminators, fast coincidence unit, CAMAC-based 16-channel time-to-digital converter, spin-tag electronics, liquid crystal retarders and their control electronics, and computer with data-acquisition card and running COBOLD analysis-and-display software. See text for details.

The temporal arrival coordinate t of the electron instigating each cascade is deduced from a fast pulse derived from the back of the second microchannel plate in each pair. This pulse is first amplified by a separate timing amplifier (ORTEC model AN 302/NL), and then presented to a constant-fraction discriminator (ORTEC model 934) which produces a time-correlated fast output pulse. For each analyzer, the five fast pulses (one for time and four for position determination) are first time delayed through 40 m of low-loss cable before being measured by a 16-channel 12 bit time-to-digital converter (TDC) (Phillips model 7186). This unit determines the arrival time of pulses in each channel relative to a common time reference, which in the present

case is related to the time-of-creation for each detected $(e,2e)$ electron pair time of ionization in the following manner.

The discriminator-output pulses, corresponding to signals from the back of each microchannel-plate pair, are presented as inputs to a fast coincidence unit (Canberra model 2144A). This unit produces an output pulse only when two pulses, one from each analyzer, arrive within 50 ns of one another. This provides a necessary, but not sufficient, condition to identify electron pairs derived from single $(e,2e)$ ionization events. The coincidence-unit output pulse, time correlated to its respective input signal, passes through a 10 m cable to the "common start" input of the TDC. This pulse initiates the TDC timing conversion process and provides a time zero against which the arrival times of the eight delay-line and two microchannel-plate timing pulses are measured. The shorter cable length used for the "common start" signal ensures that the ten individual "stop" signals arrive at a later time. The TDC produces ten 12 bit numbers which contain all information required to calculate the *x*-*y* arrival positions and arrival times for electrons measured at the two detectors. From this information, the initial momenta $(\mathbf{q}_1,\mathbf{q}_2)$ of electrons comprising each measured $(e,2e)$ event are deduced.

One additional TDC channel is employed to record the polarization state of the primary electron beam, and a second to record the polarization state of the target beam for experiments where laser-pumped, spin-polarized target atoms are employed. This is achieved using identical custom-built electronic devices which interrogate the status of the liquid-crystal controllers (Meadowlark model B1020) used to control the spin polarization states of the electron and atomic beams. Upon the detection of a coincidence event, these devices send a single pulse to their respective TDC channels, time delayed by 150 ns if the spin orientation of the beam is up, and without delay if the spin orientation is down. A counter is also employed to record the number of accumulated pulses derived from a 50 Hz pulse generator to tag measured events according to their detection time (Kinetic Systems model 3640). In summary, thirteen time coordinates are recorded for each measured $(e,2e)$ electron pair. Twelve coordinates are measured by the TDC (eight used to derive electron arrival positions, two used to record the electron arrival-time coordinates and two used to record the polarization states of the electron and atomic beams) and one coordinate is derived from a counter to time-stamp $(e,2e)$ events.

The TDC and counter are controlled through a CAMAC crate employing a custom-built RoentDek crate controller and personal computer (PC) interface card. Data acquisition, analysis, and display are performed using "COBOLD"[56] software which is run on a 600 MHz computer. The software records the coordinated data in a so-called "list-mode" format, whereby the association between these thirteen coordinate values for each recorded $(e,2e)$ event is preserved. COBOLD allows the user to incorporate custom-written C++ software (written within VISUAL STUDIO) to calculate parameters of physical relevance from the raw experimental data, for example, the emission angles and emission energies (E_1,ϕ_1) and (E_2,ϕ_2) describing $(e,2e)$ electron pairs.

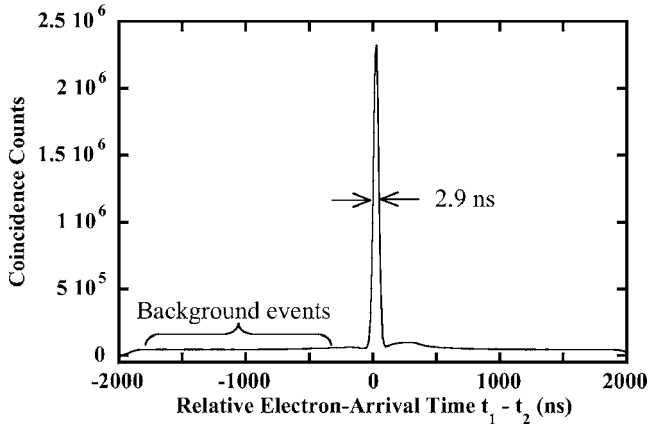

FIG. 14. Coincidence-timing spectrum measured for analyzer pass energies E_0 of 60 eV and deceleration ratios $\delta_7=1.0$. $(e,2e)$ coincidence counts are displayed as a function of the time difference t_1-t_2, where t_1 and t_2 represent the respective arrival times for the two electrons comprising each recorded electron pair. See text for details.

Figure 14 shows a typical flight-time-corrected coincidence-timing spectrum, in this case for the ionization of ground-state helium atoms where both analyzers are set to a pass energy E_0 of 60 eV. The spectrum shows coincidence counts as a function of t_1-t_2, where t_1 and t_2, respectively, represent arrival times for electrons comprising each coincident electron pair, after correction has been made for the electron energy-dependent flight-time variations through the analyzers.[3,44] Evident is a prominent peak (2.9 ns FWHM), corresponding to electrons derived from common ionization events, superimposed on a background due to electrons derived from separate ionization events. Subtraction of these background events is performed in software using standard statistical techniques. The width of the coincidence peak can be largely attributed to variations in the flight times for electrons entering the analyzers with the same entrance energy E_a, but with slightly different values of entrance angles α_a.

VI. ENERGY RESOLUTION

The predicted analyzer energy resolution from simulation is between 0.6% and 1.6% of pass energy E_0. This was calculated for an interaction volume of extent $\Delta_z=1.0$ mm measured along the z axis, for an extension $\Delta_{\text{axial}}=2.0$ mm in the axial plane, for unequal pass energies between the two toroidal-sector electrode pairs, and for values for the deceleration ratio $\delta_7=E_i/E_0$ ranging from 0.25 to 12.0. To date, measurement has only been performed in the range $0.9<\delta_7<3.3$ and for $\Delta_z=0.7$ mm. In all cases, a measured energy resolution of better than 1% has been recorded. These values compare favorably to the value of 1% predicted by Eq. (4) for an analyzer based around a single-toroidal-sector electrode pair, for an image dimension of 0.8 mm at the analyzer entrance, for a value of 1.4° for $\alpha_{\max}$ and using a value for $\kappa(c)$ of 0.30.

Figure 15 shows the detector image resulting from the measurement of elastically scattered electrons from helium at energies E_i of 55 to 66 eV at intervals of 1 eV and for equal measurement times. For this case, the average value of deceleration ratio δ_7 is close to 1.0, corresponding to the ana-

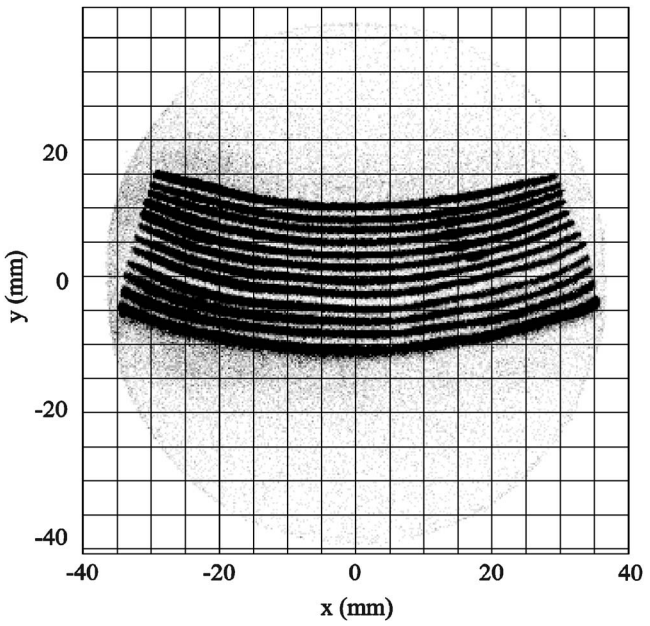

FIG. 15. Detector image resulting from the measurement of electrons scattered elastically from helium. The electron energy E_i was stepped from 55 to 66 eV at intervals of 1.0 eV. Electrons of a given energy trace out an arc on the detector. The radius of the arc varies monotonically with electron energy while the angular position along each varies linearly with the azimuthal electron-emission angle ϕ. See text for details.

lyzer pass energy value E_0=60 eV. Electrons of a given energy produce an image on the detector in the form of an arc whose origin is the cylindrical-symmetry axis for the toroidal analyzers (z axis). The angular position along each arc varies linearly with the azimuthal emission angle ϕ (each detector spanning a 40° azimuthal range), while the dispersion of arrival position with energy E_i is a monotonic nonlinear function. Energy calibration is achieved by recording the radial position of counts on the detector as a function of E_i. This is performed after conversion from (x,y) to (r,ϕ) coordinates within the software where r is radial distance measured from the z axis to the (x,y) electron arrival position on the detector. In the figure, the thickness of the lines in the radial direction (approximately 600 meV FWHM) results from the combined effects of analyzer resolution and the intrinsic energy spread of our polarized-electron beam (~300 meV). Thus, the line thickness represents an upper limit to the actual analyzer energy resolution.

VII. AZIMUTHAL-PLANE ANGULAR RESOLUTION

Toroidal-sector analyzers, which accept electrons over a broad range of azimuthal angles, possess angular-resolving properties distinctly different from those of traditional cylindrical or hemispherical analyzers employing entrance lenses of cylindrical symmetry.[7,57]

A positive ramification of the broad angular acceptance is that, if analyzer edge effects are neglected and a reasonably localized interaction-volume is assumed the analyzer transmission will, to first order, be independent of azimuthal electron-emission angle, irrespective of the symmetry of the interaction volume. Small distortions to the shape of measured electron angular distributions may still occur through second-order effects as the dimensions of the trace left on the detector corresponding to electrons emitted into a particular angle ϕ will be ϕ dependent if the interaction volume is not cylindrically symmetric about the z axis. This will express itself as a ϕ dependence in angular resolution. However, for a well-designed toroidal-sector electron analyzer, this effect should be small and have little effect on the shape of measured angular distributions unless the azimuthal cross section varies rapidly over a small angular range.

However, the fact that toroidal-sector analyzers possess a large angular acceptance in the axial plane has the negative consequence that they also efficiently measure electrons emitted from positions well removed from the interaction volume. Thus, electrons scattered from background gas along the length of the electron beam and/or electrons scattering first from the target gas, followed by additional collisions with surrounding metal surfaces (multiple-scattered electrons), may also contribute to measured spectra. Such electrons may even collide with the edges of the analyzer, where they may either be collected or result in electrons reflected back onto the detector. In any case, they will arrive at detector coordinates from which their emission angles will be inaccurately inferred. While such problems can be minimized by the use of large vacuum pumps and/or a differentially pumped target chamber and an open design for the interaction-volume surrounds, they will always be present to some degree.

In light of the above considerations, to assess the performance of the present device, both in terms of angular resolution *and* the reliability of angular distributions it measures, two different measurements were made.

Firstly, we measured the relative differential cross section for elastic scattering of electrons from argon atoms at an electron impact energy E_p of 50 eV. These results are shown as open circles in Fig. 16. For this atomic target and electron impact energy there exists a pronounced minimum in the elastic differential cross section between scattering angles of 60°–80° which can be used to assess the quality of azimuthal-plane angular resolution. At these azimuthal scattering angles, the ±1.4° angular acceptance of the toroidal lens system in the radial planes results in negligible broadening of measured angular structure, and, hence, the width of measured minimum can be directly interpreted in terms of the azimuthal-plane angular resolution of the analyzer. As described in Sec. III F, the angular resolution of toroidal analyzers is not only a function of the chosen c parameter, but also of the spatial extent Δ_{axial} of the interaction volume in the axial plane and the chosen lens and toroidal-sector electrode operating voltages. For the present measurement, an analyzer pass energy E_0 of 50 eV was chosen, corresponding to a lens deceleration value δ_7 of 1.0. Under such conditions and with appropriate lens potentials applied, our simulation predicted an azimuthal angular resolution of 2° FWHM. In the majority of cases, larger values of δ_7 lead to degraded levels of angular resolution, although improvements may be encountered for certain specific lens-potential values, as discussed in Sec. III E 4.

The present results are compared to the ±1.5° angular resolution measurements of Panajotovic *et al.*[58] who quote a

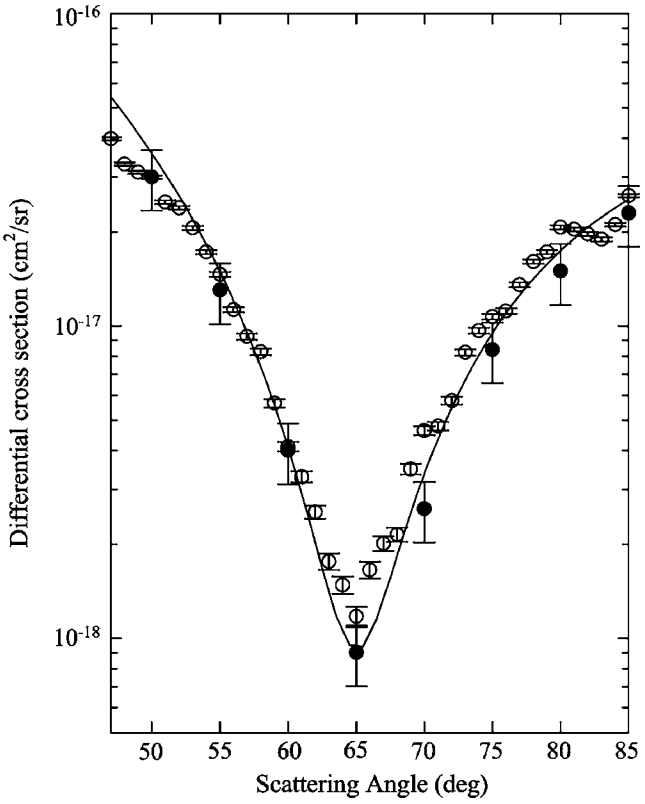

FIG. 16. Differential cross section for electrons elastically scattered from argon at an impact energy of 50 eV. Open circles: present results. Solid circles: experimental results of Panajotovic *et al.* (Ref. 58). Solid line: relativistic polarized-orbital calculation by McEachran (Ref. 59) convoluted with a 2° FWHM Gaussian. The present results have been normalized to the data of Panajotovic *et al.* at a scattering angle of 50°.

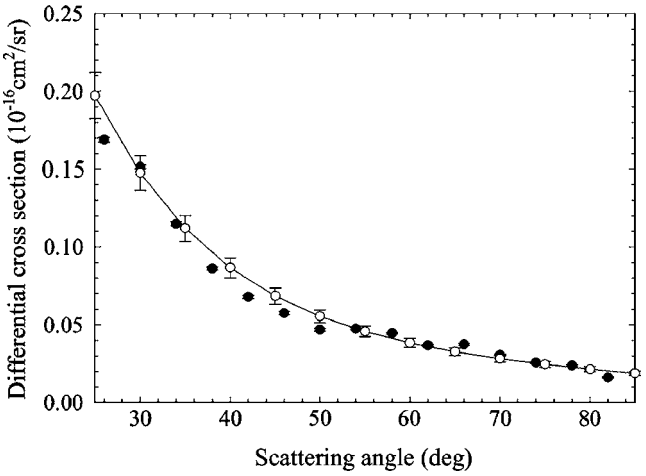

FIG. 17. Measured angular distribution for elastic scattering from helium at 100 eV. Solid circles: present results. Open circles connected by straight lines: experimental results of Register *et al.* (Ref. 60). Large scatter in present data points primarily attributable to spatial gain variations in microchannel-plate detection efficiency. See text for details.

total error of 22% in their normalized cross sections (filled circles). For those measurements, they employed a single-channel hemispherical analyzer. Therefore, comparison of the present data with theirs provides a good test to the actual angular resolution of our toroidal-sector device. As the present measurement of cross sections is not absolute, we have normalized our data to that of Panajotovic *et al.* at a scattering angle of 50°. This angle was selected because the cross section is relatively high at that point and its dependence on scattering angle is weak in that neighborhood, rendering the normalization process less sensitive to any differences in angular resolution between the present and previous measurements. Overall, there is good agreement between the two data sets over the entire angular range although some deviations falling outside of the quoted error bars are evident. This level of agreement gives us confidence that the predicted 2° FWHM angular resolution value has been well approximated. Furthermore, it implies that scattering from background gas along the length of the electron beam does not significantly contribute to the shape of the present angular distribution, for if it did, the deep minimum at 65° would have been measured as a much shallower structure than was measured by Panajotovic *et al.* whose spectrometer, by nature of its cylindrical-symmetry optics, does not suffer from this problem. Also shown on Fig. 16 is a relativistic polarized-orbital calculation by McEachran,[59] which includes both static- and dynamic-polarization potentials as well as an *ab initio* absorption potential. The results have been convoluted with a Gaussian of width of 2°. Overall there is quite a good agreement with our experimental data, again consistent with the 2° analyzer resolution predicted by our simulation.

Evident in the present results is a degree of scatter in the data points, particularly above 65°, exceeding that to be expected from their associated error bars which were calculated from statistical considerations only. While this scatter is primarily attributable to variations in microchannel-plate detection efficiency in the present case, azimuthal variations in the analyzer transmission resulting from mechanical misalignment or buildup of contaminants on the electron optics may also contribute, as may the detection of multiple-scattering events or the presence of stray magnetic fields. We note that, at the time of this measurement, our microchannel-plate detectors were rather old and exhibited strong point-to-point variations in detector efficiency. However, we choose here to show the reader our raw data to demonstrate the size of corrections which may need to be applied for such a spectrometer.

Secondly, we measured the angular distribution for elastic scattering from helium at 100 eV. This cross section has been previously measured[60] and calculated[61] to high accuracy and is known to vary smoothly with emission angle. It is therefore well suited to both assess the performance of our analyzer angular response and provide corrections to it. Figure 17 shows our results (solid circles) compared to those of Register *et al.*[60] (open circles). To aid visual comparison, the data points of Register *et al.* are joined by straight lines. The present data, being relative, are normalized to those of Register *et al.* at 54°. Overall, there is a good agreement between the two data sets. Once again, however, the degree of scatter in the present data points exceeds that expected from the indicated error bars, which were calculated from statistical considerations only, and is primarily attributable to variations in microchannel-plate detection efficiency.

To accurately correct the angular response of toroidal-

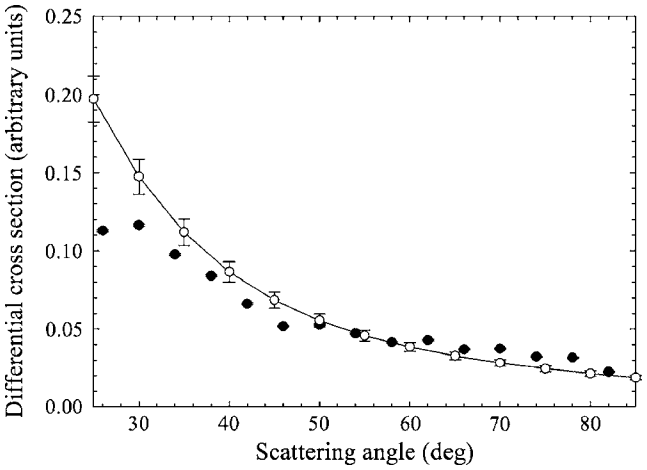

FIG. 18. Elastic scattering measurement from background helium gas. Experimental conditions as for Fig. 17, except that the target gas is introduced from a position well removed from the z axis.

sector analyzers using high-quality elastic cross sections derived from previous studies, the measured spectra must not contain substantial contributions from either of the two mechanisms: (a) multiple-scattering processes or (b) electron collisions with background gas. Both of these scenarios were discussed earlier in this section.

The magnitude of contributions from mechanism (a), which result in a target-gas-related "background" structure, is generally very difficult to quantify, not only in the present design but for electron spectrometers in general. The authors therefore suggest minimizing this effect by coating all exposed surface in the vicinity of the interaction volume with materials characterized by low levels of secondary electron emission and by maximizing the electrode-free volume surrounding the interaction region. We also note that, while some unusual structures were evident in our measured spectra in the early stage of our spectrometer development, the introduction of slit A_{4b} (see Fig. 9) into our focusing lens (which was not in the original design) greatly suppressed these structures by removing off-axis electron trajectories which could not have originated from a single-scattering events at the interaction region. Thus, careful thought to the provision of strategically located antiscattering slits in future lens designs is recommended.

In contrast, the magnitude and angular dependence of contributions from mechanism (b) can be estimated by comparing measurements, taken for the same background pressure and measurement time, with the target gas, respectively, admitted into the interaction volume through the target-gas needle (at position $x=y=z=0$) and admitted into the scattering chamber at a position well removed from the z axis. Figure 18 shows such a comparison made by us by performing an additional elastic-scattering measurement, under identical conditions to that of Fig. 17, except from background helium gas. The present results are again compared to those of Register *et al.*[60] and normalized to the latter at 54°. Firstly, we note that the count rate for the background measurement of Fig. 18 was less than 5% of the rate for the measurement of Fig. 17, illustrating that these contributions are relatively small for the present spectrometer design. The small size of this contribution is in spite of the fact that the present design employs a nondifferentially pumped effusive-target source for which higher background contributions will occur in comparison to differentially pumped supersonic beam systems.[2] Secondly, and rather interestingly, the shape of the measured angular distributions in both figures is not too dissimilar over a significant portion of the angular range, illustrating some residual parallel-to-point focusing capability even for substantially off-axis rays. Below 40°, however, larger differences are evident. This is not surprising as vignetting of electrons derived from severely off-axis locations is expected as the forward azimuthal-acceptance limit at $\phi=20°$ is approached. Taken together, the similarity of the two angular distributions over most of the angular range and the low background levels suggest that contributions from scattering along the length of the electron beam does not significantly distort angular distributions in the present design.

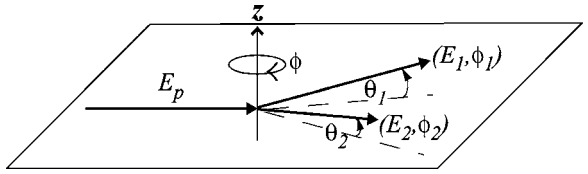

FIG. 19. Schematic representation of scattering geometry and coordinate system defining the $(e,2e)$ triple-differential ionization cross section. An incident electron of energy E_i ionizes a target atom, resulting in the ejection of two electrons of respective energies E_1 and E_2 into the polar and azimuthal emission angles θ_1 and θ_2, and ϕ_1 and ϕ_2, respectively. For the present spectrometer design, only those electron pairs emitted into a common plane $\theta_1=\theta_2=0°$ containing the incident electron trajectory (the so-called scattering plane) are measured.

VIII. EFFICIENCY CORRECTIONS FOR $(e,2e)$ DATA

The so-called triple-differential cross section $d^5\sigma/d\Omega_1 d\Omega_2 dE_2$ is a measure of the probability that an $(e,2e)$ ionization event will occur when an incident electron of energy E_p produces two electrons of energies E_1 and E_2 scattered, respectively, into the solid angles $d\Omega_1(\theta_1,\phi_1)$ and $d\Omega_2(\theta_2,\phi_2)$. The reaction kinematics is shown schematically in Fig. 19, with angles θ_i, $i=1,2$, and ϕ_i, $i=1,2$, respectively measured out of and in the axial plane. For the present spectrometer design, only electrons emitted into the common plane $(\theta_1=\theta_2=0°)$ are measured. Furthermore, the spectrometer described in this article can only determine *relative* ionization cross sections, because factors such as the target and electron beam density variations across the interaction volume, the absolute detection efficiencies of the electron detectors, and the transmission efficiency for electrons traveling through the analyzers are not determined. This additional information would be required to directly relate the measured count rates to the triple-differential cross section.[1] However, the spectrometer can determine the relative variations of $d^5\sigma/d\Omega_1 d\Omega_2 dE_2$ as a function of the emission angles ϕ_1 and ϕ_2 and energies E_1 and E_2, over the analyzer acceptance ranges $\Delta\phi_1$, $\Delta\phi_2$, ΔE_1, and ΔE_2, if variations in detection efficiency with the angular and energy variables are taken into account. This is achieved in the following manner.

For a given impact energy E_p, the measured $(e,2e)$ count rate $N(E_1,E_2,\phi_1,\phi_2)$ can be explicitly related to the triple-differential cross section $d^5\sigma/d\Omega_1 d\Omega_2 dE_2$ through the expression

$$d\sigma/d\Omega_1 d\Omega_2 dE_2 = f(\rho_e,\rho_g)N(E_1,E_2,\phi_1,\phi_2)/\varepsilon(E_1,E_2,\phi_1,\phi_2). \tag{6}$$

Here, f is a function dependent upon the magnitudes and spatial density profiles of the incident electron beam ρ_e and target gas ρ_g across the interaction volume. $\varepsilon(E_1,E_2,\phi_1,\phi_2)$ is a function representing the absolute detection efficiency of the spectrometer for $(e,2e)$ electron pairs emitted into the phase-space volume $d\Omega_1 d\Omega_2 dE_2$. Here, $\varepsilon(E_1,E_2,\phi_1,\phi_2)=1.0$ is defined as 100% detection efficiency for two coincident electrons emitted into the respective phase-space coordinates (E_1,ϕ_1) and (E_2,ϕ_2).

For the present spectrometer (excluding fringe-field effects), one would expect ε to be independent of ϕ_1 and ϕ_2 due to the partial cylindrical symmetry of the toroidal-sector analyzers. In practice, ϕ_1- and ϕ_2-dependent variations in ε are observed. As described in Sec. VII, these may arise from the presence of stray magnetic fields or from inaccuracies in mechanical alignment. A weak dependence in ε on E_1 and E_2 also occurs due to small energy-dependent transmission variations in the first stage of the focusing lenses. Spatial variations in the two analyzers' microchannel-plate detection efficiencies also introduce additional E and ϕ-dependent variations in ε. However, if $\varepsilon(E_1,E_2,\phi_1,\phi_2)$ can be determined (or a quantity proportional to it) for a given interaction-volume geometry $f(\rho_e,\rho_g)$, then the measured $(e,2e)$ count rates can be related to the triple-differential cross section through a single normalization constant. This we achieve through the procedure described below, which relies on theoretically determined elastic scattering cross sections for helium, whose accuracy is well established.[62]

Firstly, it is noted that the function $\varepsilon(E_1,E_2,\phi_1,\phi_2)$, which applies to the detection of two electrons in coincidence, can be expressed as a product of two independent efficiency functions $\varepsilon_1(E_1,\phi_1)$ and $\varepsilon_2(E_2,\phi_2)$, each dependent only upon the properties of a single analyzer, i.e.,

$$\varepsilon(E_1,E_2,\phi_1,\phi_2) = \varepsilon_1(E_1,\phi_1)\varepsilon_2(E_2,\phi_2). \tag{7}$$

The validity of this factorization rests on the assumption that the two analyzers are correctly aligned and "view" a common interaction volume. However, even if one analyzer is misaligned by a small displacment in the z direction, the modified relation $\varepsilon(E_1,E_2,\phi_1,\phi_2)=\eta\varepsilon_1(E_1,\phi_1)\varepsilon_2(E_2,\phi)$ will still hold, where η is a constant $(\eta\leqslant 1)$ whose value depends on the degree of overlap of both analyzers' polar angular-acceptance ranges defined in the radial planes. For this reason, accurate $(e,2e)$ efficiency corrections can still be performed with confidence through the procedure described below, even though $(e,2e)$ count rates may be severely affected through any z-axis misalignment, as the factor η cancels out. In contrast, for small misalignments in the x-y plane, Eq. (7) still holds for any well-localized interaction volume, as it will remain completely encompassed by the broad azimuthal acceptances of both analyzers.

To determine $\varepsilon_1(E_1,\phi_1)$ and $\varepsilon_2(E_2,\phi_2)$ within multiplicative factors, we record the count rates $N_{\mathrm{el}(1)}(E_1,\phi_1)$ and $N_{\mathrm{el}(2)}(E_2,\phi_2)$ for elastic scattering from helium in a noncoincidence experiment. This is undertaken by scanning the incident beam energy over the respective acceptance ranges ΔE_1 and ΔE_2 for the two analyzers and correcting the measured count rates for any energy-dependent changes in primary electron beam current. In this way, data are collected at each energy-angle coordinate for an equal time. From knowledge of the well-established, theoretically derived elastic scattering cross sections $\sigma_{\mathrm{el}}(E_1,\phi_1)$ and $\sigma_{\mathrm{el}}(E_2,\phi_2)$, the quantities $W_1(E_1,\phi_1)=N_{\mathrm{el}(1)}(E_1,\phi_1)/\sigma_{\mathrm{el}}(E_1,\phi_1)$ and $W_2(E_2,\phi_2)=N_{\mathrm{el}(2)}(E_2,\phi_2)/\sigma_{\mathrm{el}}(E_2,\phi_2)$ [which are proportional to $\varepsilon_1(E_1,\phi_1)$ and $\varepsilon_2(E_2,\phi_2)$, respectively] are then calculated and recorded in two histograms as functions of their respective energy and angular coordinates. The corrected $(e,2e)$ spectrum, proportional to the quantity of interest $d^5\sigma/d\Omega_1 d\Omega_2 dE_2$ of Eq. (6), is then simply formed from the expression $N(E_1,E_2,\phi_1,\phi_2)/W(E_1,E_2)W_2(E_2,\phi_2)$.

Again, it is emphasized that such a technique will only be valid if the measured elastic data used to correct the $(e,2e)$ spectra are free from multiple-scattered electrons or from scattered electrons derived from locations well removed from the axis of cylindrical symmetry. Such contributions lead to electrons focused to positions on the detector where their momenta are inaccurately deduced.

It should also be stressed that before adopting the above procedure, an angular calibration of both analyzers should be performed, as any misalignments may lead to nonlinearities and offsets in the angular scale. In the present case, the linearity of the angular scale was established by introducing a series of equally spaced circular apertures in front of the analyzers' lens systems at known angular positions, and spectra for elastic scattering from helium were recorded. Duguet *et al.*[39] describe a similar procedure in detail. The equal angular spacing of peaks measured on the detectors established that linearity in azimuthal response had indeed been achieved in the present case. However, even if nonlinearities are observed in such a calibration measurement, these can be corrected for in software. This procedure, however, does not take into account any perturbations to electron trajectories due to any unaccounted for stray fields which might exist between the interaction volume and the circular apertures employed for angular calibration.

IX. $(e,2e)$ RESULTS

The efficiency of the present spectrometer is illustrated in Fig. 20. Here, the relative $(e,2e)$ cross section is presented for the ionization of ground-state helium atoms where the residual He^+ is excited to the $n=3$ manifold. The incident beam energy was 317 eV and the beam current was 20 nA. Fast scattered electrons were simultaneously collected over the energy band spanning 193–207 eV (mean energy of 200 eV) and slow scattered electrons over the energy band spanning 37–51 eV (mean energy of 44 eV). The analyzer pass energies were 70 eV. The spectrum comprises around 28 000 coincidence counts and the total data-collection time was around 2 days, corresponding to a signal rate of around

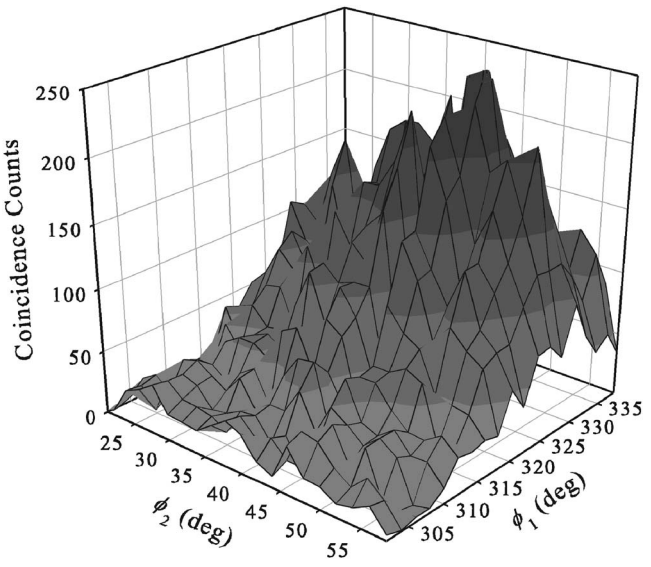

FIG. 20. Relative $(e,2e)$ cross section for the ionization of ground-state helium where the residual He^+ ion is excited to the $n=3$ manifold. The incident beam energy was 317 eV, the fast and slow scattered electrons of 200 and 44 eV respective mean energies. For these kinematics, ionization leading to this excited state is around 0.4% of the intensity of $(e,2e)$ transitions leaving the residual ion in the ground state. Data-collection time was around 2 days. See text for details.

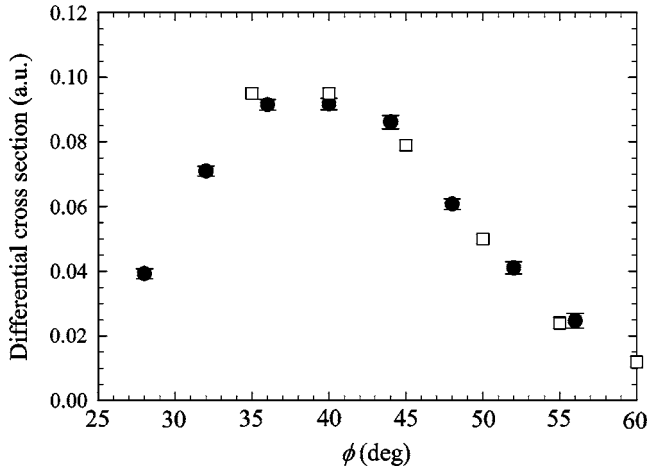

FIG. 21. Doubly symmetric $(e,2e)$ measurement on helium where the residual ion is left in the ground electronic state. Incident beam energy $E_i = 104$ eV, electron scattering angles $\phi_1 = \phi_2 = \phi$. Solid circles: present data, open squares: Murray and Read (Ref. 63). Present data have been normalized to Murray and Read data for best visual fit. Error bars on Murray and Read data not shown as they are smaller than symbols. See text for details.

0.16 Hz. For the chosen kinematics, ionizing transitions leading to $n=3$ manifold comprise around 0.4% of the intensity of those leaving the residual ion in the ground state, demonstrating the high sensitivity of the present device.

The efficacy of the detection-efficiency correction procedure for $(e,2e)$ data, described in Sec. VIII, is assessed in Fig. 21. Here, we have performed a coplanar doubly symmetric $(e,2e)$ measurement on helium where the residual ion is left in the ground electronic state. Our results are compared to the results of Murray and Read[63] obtained using a single-channel $(e,2e)$ electron spectrometer, for which obtaining accurate angular distributions should, in principle, be less complicated than for multiparameter electron spectrometers such as the present device. The present data, with efficiency corrections made using the procedure outlined in Sec. VIII and employing elastic cross section of Register *et al.*,[60] have been normalized to that of Murray and Read for best visual comparison. As can be seen, there is very good agreement between the angular distributions measured with two very different spectrometer designs. Given that the corrections which needed to be applied were not insubstantial (as can be seen from the point-to-point angular variations in the *uncorrected* data of Fig. 17), the degree of agreement in the present figure gives confidence to our adopted correction procedure and confidence in the ability of the present spectrometer to measure reliable angular distributions, even when significant point-to-point gain variations in the position-sensitive detectors are present.

X. CONCLUSION

To design an electron spectrometer of the highest sensitivity requires the adoption of multiparameter data-collection techniques, in which simultaneous measurement is made over a large volume of momentum phase space with high momentum resolution. In this article we describe the design, construction, and operation of a new multiparameter $(e,2e)$ electron spectrometer. We have quantified its performance, drawing attention to its strengths and limitations and suggesting way to further improve the design. By focusing on the underlying design principles and attendant challenges, we hope to provide a strong design framework for future generations of multiparameter electron spectrometers.

The present spectrometer consists of two analyzers of toroidal-sector geometry. Each analyzer incorporates a fast delay-line detection system and exhibits good energy ($<1\%$ of the pass energy) and angular resolutions over a range of operating conditions. For each analyzer, simultaneous measurement is performed over a 40° angular range and over an energy range corresponding to 20% of its pass energy. Through the adoption of a large cylindrical-to-spherical-radius ratio, the design achieves high angular resolution for electrons emitted from an interaction volume of a few millimeters spatial extent. By enabling simultaneous data collection over a broad range of energy and angular coordinates, improvements in $(e,2e)$ collection efficiency of greater than two orders of magnitude have been achieved in comparison to the hemispherical-analyzer-based system it replaces. As for all multiparameter electron spectrometers, correcting for non uniformities in collection efficiency over the accepted momentum phase space remains a major challenge. Likely sources for these non uniformities have been identified in the present design and a methodology for their correction has been developed. By comparing elastic and $(e,2e)$ data on helium with previous measurements, we have demonstrated the capacity of the present device to measure reliable angular distributions in coincidence studies.

While the present design exhibits high performance, room exists for further improvements. Improved energy resolution could be gained through the adoption of modified-toroidal-sector electrodes of noncircular cross section and an

improved choice of toroidal-sector deflection angles. Adoption of a differentially pumped target beam, for example, by employing a supersonic beam source, would reduce background contributions. Furthermore, recent simulations by the authors suggest that significant improvements in analyzer transmission can be achieved through modifications to the entrance optics without sacrifice to energy resolution. Those results will appear in a later publication.

ACKNOWLEDGMENTS

We thank J. Williams and P. Hayes for interesting discussions in the early stages of the analyzer design. We also thank A. Dorn, H. Schmidt-Böcking, M. Smolarski, C. Höhr, A. Knapp, M. Hattas, and K. Ullmann-Pfleger for stimulating discussions and their contributions to this work. We also acknowledge the technical expertise of Mr. Kevin Roberts who constructed large portions of the spectrometer and provided valuable design input. The assistance of the Australian-German Research Cooperation Scheme and the Australian Research Council through Grant No. DP0452553 and a 1998 ARC RIEF grant is gratefully acknowledged.

[1] E. McCarthy and E. Weigold, *Electron-Atom Collisions* (Cambridge University Press, Cambridge, England, 1995).
[2] J. Ullrich, R. Moshammer, A. Dorn, R. Dörner, L. Ph. H. Schmidt, and H. Schmidt-Böcking, Rep. Prog. Phys. **66**, 1463 (2003).
[3] J. Lower and E. Weigold, J. Phys. E **22**, 421 (1989).
[4] H. Ehrhardt, M. Schulz, T. Tekaat, and K. Willmann, Phys. Rev. Lett. **22**, 89 (1969).
[5] R. Camilloni, A. Giardini-Guidoni, R. Tiribelli, and G. Stephani, Phys. Rev. Lett. **29**, 618 (1972).
[6] J. P. D. Cook, I. E. McCarthy, A. T. Stelbovics, and E. Weigold, J. Phys. B **17**, 2339 (1984).
[7] S. D. Kevan, Rev. Sci. Instrum. **54**, 1441 (1993).
[8] J. H. Moore, M. A. Coplan, L. Skillmann, Jr., and E. D. Brooks III, Rev. Sci. Instrum. **49**, 463 (1978).
[9] B. R. Todd, N. Lermer, and C. E. Brion, Rev. Sci. Instrum. **65**, 349 (1994).
[10] P. Storer, R. S. Caprari, S. A. C. Clark, and E. Weigold, Rev. Sci. Instrum. **65**, 2214 (1994).
[11] C. Miron, M. Simon, N. Leclercq, and P. Morin, Rev. Sci. Instrum. **68**, 3728 (1997).
[12] M. Takahashi, T. Saito, M. Matsuo, and Y. Udagawa, Rev. Sci. Instrum. **73**, 2242 (2002).
[13] A. Danjo, Y. Kato, N. Kobayashi, J. Matsumoto, H. Shimizu, H. Tanuma, Z. Wang, W. Wu, K. Yamazaki, and M. Yoshino, Rev. Sci. Instrum. **70**, 1970 (1999).
[14] X. G. Ren, C. G. Ning, J. K. Deng, S. F. Zhang, G. L. Su, F. Huang, and G. Q. Li, Rev. Sci. Instrum. **76**, 063103 (2005).
[15] M. Takahashi, N. Watanabe, Y. Khajuria, K. Nakayama, Y. Udagawa, and J. H. D. Eland, J. Electron Spectrosc. Relat. Phenom. **141**, 83 (2004).
[16] F. Catoire, E. M. Staicu-Casagrande, A. Lahmam-Bennani, A. Duguet, A. Naja, X. G. Ren, B. Lohmann, and L. Avaldi, Rev. Sci. Instrum. **78**, 013108 (2007).
[17] R. Dörner, V. Mergel, O. Jagutzki, L. Spielberger, J. Ullrich, R. Moshammer, and H. Schmidt-Böcking, Phys. Rep. **330**, 95 (2000).
[18] X. Guo, J. M. Hurn, J. Lower, S. Mazevet, Y. Shen, E. Weigold, B. Granitza, and I. E. McCarthy, Phys. Rev. Lett. **76**, 1228 (1996).
[19] A. Dorn, A. Elliott, J. Lower, S. F. Mazevet, R. P. McEachran, I. E. McCarthy, and E. Weigold, J. Phys. B **31**, 547 (1998).
[20] E. Weigold and I. E. McCarthy, *Electron Momentum Spectroscopy* (Kluwer Academic, New York, 1999).
[21] J. S. Risley, Rev. Sci. Instrum. **43**, 95 (1972).
[22] H. Z. Sar-el, Rev. Sci. Instrum. **38**, 1210 (1967).
[23] E. M. Purcell, Phys. Rev. **54**, 818 (1938).
[24] C. E. Kuyatt and J. A. Simpson, Rev. Sci. Instrum. **38**, 103 (1967).
[25] H. Wollnik, *Focussing of Charged Particles*, edited by A. Septier (Academic, New York, 1967), Vol. 2, pp. 164–202.
[26] F. Toffoletto, R. C. G. Leckey, and J. D. Riley, Nucl. Instrum. Methods Phys. Res. B **12**, 282 (1985).
[27] T. J. Reddish, G. Richmond, G. W. Bagley, J. P. Wightman, and S. Cvejanovíc, Rev. Sci. Instrum. **68**, 2685 (1997).
[28] H. Goldstein, *Classical Mechanics*, 2nd ed. (Addison-Wesley, Reading, MA, 1980).
[29] SIMION, ion source software, P.O. Box 2726 Idaho Falls, ID 83404, USA.
[30] R. C. G. Leckey and J. D. Riley, Appl. Surf. Sci. **22/23**, 196 (1985).
[31] R. C. G. Leckey, J. Electron Spectrosc. Relat. Phenom. **43**, 183 (1987).
[32] G. J. A. Hellings, H. Ottevanger, C. L. C. M. Knibbeler, J. Van Engelshoven, and H. H. Brongersma, J. Electron Spectrosc. Relat. Phenom. **49**, 359 (1989).
[33] R. G. Smeek, R. M. Tromp, H. H. Kersten, A. J. H. Boerboom, and F. W. Saris, Nucl. Instrum. Methods Phys. Res. **195**, 581 (1982).
[34] M. R. F. Siggel-King, R. Lindsay, F. M. Quinn, J. Pearson, G. Fraser, and G. Thornton, J. Electron Spectrosc. Relat. Phenom. **137**, 721 (2004); M. R. F. Siggel-King, R. Lindsay, T. J. Reddish, D. P. Seccombe, and F. M. Quinn, *ibid.* **144**, 1005 (2005).
[35] C. Azimonte, A. R. B. de Castro, A. Tadich, J. D. Riley, and R. C. G. Leckey, Braz. J. Phys. **33**, 788 (2003).
[36] J. H. Flexman, J. F. Williams, and P. A. Hayes, J. Phys. IV **3**, 79 (1993).
[37] R. W. van Boeyen and J. F. Williams, Rev. Sci. Instrum. **76**, 063303 (2005).
[38] J. Matsumoto, N. Kobayashi, A. Danjo, and M. Yoshino, Rev. Sci. Instrum. **75**, 360 (2004).
[39] A. Duguet, A. Lahmam-Bennani, M. Lecas, and B. El Marji, Rev. Sci. Instrum. **69**, 3524 (1998).
[40] R. Guillemin, E. Shigemasa, K. Le Guen, D. Ceolin, C. Miron, N. Leclercq, K. Ueda, P. Morin, and M. Simon, Rev. Sci. Instrum. **71**, 4387 (2000).
[41] K. Le Guen, D. Céolin, R. Guillemin, C. Miron, N. Leclercq, M. Bougeard, M. Simon, P. Morin, A. Mocellin, F. Burmeister, A. Naves de Brito, and S. L. Sorensen, Rev. Sci. Instrum. **73**, 3885 (2002).
[42] H. A. Engelhardt, A. Zartner, and D. Menzel, Rev. Sci. Instrum. **52**, 835 (1981).
[43] J. Moore, C. C. Davis, and M. Coplan, *Building Scientific Apparatus* (Addison-Wesley, Reading, MA, 1983), p. 288.
[44] P. Hayes, M. A. Bennett, J. Flexman, and J. F. Williams, Rev. Sci. Instrum. **59**, 2445 (1988).
[45] E. Harting and F. H. Read, *Electrostatic Lenses* (Elsevier, Amsterdam, 1976).
[46] S. Ramo, J. Whinnery, and T. van Duzer, *Fields and Waves in Communication Electronics* (Wiley, New York, 1965), p. 168.
[47] D. T. Pierce, R. J. Celotta, G.-C. Wang, W. N. Unertl, A. Galejs, C. E. Kuyatt, and S. R. Mielczarek, Rev. Sci. Instrum. **51**, 478 (1980).
[48] P. A. Hayes, D. H. Yu, and J. F. Williams, Rev. Sci. Instrum. **68**, 1708 (1997).
[49] C. D. Schröter, A. Rudenko, A. Dorn, R. Moshammer, and J. Ullrich, Nucl. Instrum. Methods Phys. Res. A **536**, 312 (2005).
[50] J. Kessler, *Polarized Electrons*, 2nd ed. (Springer, Berlin, 1985).
[51] Electronic Material Engineering, RSPhysse, Australian National University, http://wwwrsphysse.anu.edu.au/eme/home.php
[52] T. Nakanishi, H. Aoyagi, H. Horinaka, Y. Kamiya, T. Kato, S. Nakamura, T. Saka, and M. Tsubata, Phys. Lett. A **158**, 345 (1991).
[53] J. Lower, A. Elliott, E. Weigold, S. Mazevet, and J. Berakdar, Phys. Rev. A **62**, 012706 (2000).
[54] N. Anderson, J. W. Gallagher, and I. V. Hertel, Phys. Rep. **165**, 1 (1988).
[55] J. L. Wiza, Nucl. Instrum. Methods **162**, 587 (1979).
[56] Roentdek Gmbh, www.roentdek.com
[57] R. T. Brinkmann and S. Trajmar, J. Phys. E **14**, 245 (1981).
[58] R. Panajotovic, D. Filipovic, B. Marinkovic, V. Pejcev, M. Kurepa, and L. Vuskovic, J. Phys. B **30**, 5877 (1997).
[59] R. P. McEachran (private communication).
[60] D. F. Register, S. Trajmar, and S. K. Srivasta, Phys. Rev. A **21**, 1134 (1980).
[61] D. V. Fursa and I. Bray, J. Phys. B **30**, 757 (1997).
[62] I. Bray (private communication).
[63] A. J. Murray and F. H. Read, J. Phys. B **25**, L579 (1992).